NTNU
Norwegian University of
Science and Technology

Numerical solution of buoyancy-driven flow problems

Einar Rossebø Christensen

Master of Science in Physics and Mathematics
Submission date: June 2009
Supervisor: Einar Rønquist, MATH

Norwegian University of Science and Technology
Department of Mathematical Sciences

Problem Description

A computational procedure for solving the time-dependent, incompressible Navier-Stokes equations based on spectral methods in space and operator splitting methods in time should first be implemented and tested.
The computational procedure should then be applied to solve buoyancy-driven flow problems, and the numerical results should be compared with relevant results from linear stability theory, other numerical results, and experimental observations.

Assignment given: 19. January 2009
Supervisor: Einar Rønquist, MATH

Preface

This thesis concludes my five-year study of physics and applied mathematics at the Norwegian University of Science and Technology in Trondheim, Norway. The thesis has been carried out at the Department of Mathematical Sciences under the subject code TMA4910, and constitutes an equivalence of 30 ECTS points.

All numerical simulations are carried out in Matlab - a programming tool I consider as excellent for both numerical analysis and visualization of numerical results.

I would like to thank my supervisor, Professor Einar M. Rønquist, at the Department of Mathematical Sciences, NTNU. His good ideas and encouraging feedback has meant a lot during the entire semester.

Trondheim, 15th June, 2009
Einar Rossebø Christensen

Abstract

Numerical solution of buoyancy-driven flow problems in two spatial dimensions is presented. A high-order spectral method is applied for the spatial discretization, while the temporal discretization is done by operator splitting methods. By solving the convection-diffusion equation, which governs the temperature distribution, a thorough description of both the spatial and the temporal discretization methods is given. A fast direct solver for the arising system of algebraic equations is presented, and the expected convergence rates of both the spatial and the temporal discretizations are verified. As a step towards the Navier–Stokes equations, a solution of the Stokes problem is given, where a splitting scheme technique is introduced. An extension of this framework is used to solve the incompressible Navier–Stokes equations, which govern the fluid flow. By solving the Navier-Stokes equations and the convection-diffusion equation as a coupled system, two different buoyancy-driven flow problems in two-dimensional enclosures are studied numerically. In the first problem, emphasis is put on the arising fluid flow and the corresponding thermal distribution, while the second problem mainly consists of determining critical parameters for the onset of convection rolls.

Contents

Chapter 1

Introduction

If a fluid is heated and the fluid density varies with temperature, a flow can be induced in the presence of gravity. This is known as buoyancy-driven flows. Many flow phenomena are driven by buoyancy, and such flows are important in a variety of engineering applications, e.g. ventilation in rooms, cooling of nuclear reactors and electronic components, solar energy collection and crystal growth in liquids.

In this paper we consider buoyancy-driven flows in two-dimensional enclosures. Earlier works covering such material can in general be classified into two groups: differentially heated cavities and enclosures heated from below. We will in this paper consider flows contained in both of these groups. The first problem we consider is a layer of fluid contained in a rectangular differentially heated cavity [15, 14, 13]: by applying a temperature difference between the vertical walls of the cavity, we experience onset of convection.

The second problem is the famous Rayleigh–Bénard convection. Rayleigh–Bénard convection is a type of natural convection that is produced by an unstable layer of fluid bounded by horizontal plates. The problem has been extensively studied, specially inside rectangular cavities [18, 22, 21]. The Rayleigh–Bénard convection is an important mechanism that can be found in many natural processes, e.g. geophysics, astrophysics and meteorology.

The results presented is achieved using the spectral or high-order method. The method is related to the finite element method by the fact that it uses a Galerkin approach, based on the weak statement of the governing equations. The approach is to seek a solution in a discrete space of basis functions, expressing the solution as a linear combination of these. The basis functions that span our discrete search space are high-order polynomials.

By employing the spectral method, we can obtain tremendous accuracy if the expected solution of our problem is very regular [5]. This is often the case for incompressible flow problems, and the method is therefore well suited for the flow problems considered here. If we expect a smooth solution, while the computational domain at the same time has piecewise smooth boundaries, the spectral method can provide exponential convergence as the polynomial degree is increased. The interpretation of this is that the error of the solution decays faster than any algebraic power of N, the degree of the polynomial basis. In summary, the spectral method is an excellent method if accurate solutions of regular problems on piecewise smooth domains are sought.

We start by presenting a numerical solution of the two-dimensional convection-diffusion equation. The convection-diffusion equation describes the transfer of heat inside a physical system, and will be important in the simulation of the buoyancy-driven flows. The equation is also an appropriate starting problem, where we in detail discuss the spatial and the temporal discretization methods, together with a clever approach for solving the arising system of algebraic equations.

In the next chapter, we move into the world of fluid mechanics and consider Stokes flow. This is a type of flow where the Reynolds number is small, and where transport by diffusion is dominating. The problem is coupled between fluid velocity and pressure, and we apply an operator splitting scheme introduced in [1] to solve the problem. The splitting scheme is tested on a somewhat artificial problem, i.e. a constructed problem with a known solution, and the expected convergence behaviour is verified.

Our next goal is to solve the equations that describe the fluid motion in the flow examples. We assume that the fluids considered can be modeled as incompressible Newtonian flow, i.e. flow with a constant viscosity. Hence, the flow can be modeled by the Navier–Stokes equations, which are based on conservation of mass and linear momentum. An extension of the Stokes splitting scheme is applied to these equations.

Finally, the derived framework for solving the Navier–Stokes equations is applied to the buoyancy-driven flow problems. For the differentially heated cavity, we present a study of the arising fluid flow and the corresponding heat transfer through parts of the domain boundary, quantified by the Nusselt number. In the Rayleigh–Bénard convection problem, the computed fluid flow pattern is compared to experimental observations. At the end, critical parameters of the flow are compared with relevant results from linear stability theory.

Chapter 2

The convection-diffusion equation

The convection-diffusion equation describes transfer of a physical quantity inside a physical system due to two processes: diffusion and convection. We consider here the transfer of heat (energy), where the diffusion term can be considered as dispersion of heat (conduction), while convection describes the heat carried by a velocity field, e.g. the interaction of fluid flow and heat.

In this chapter we give a numerical solution of the two-dimensional unsteady convection-diffusion equation. This will be an appropriate starting problem to show how we handle time-dependent partial differential equations, in particular, the spatial and temporal discretization of such equations.

2.1 Strong and weak form

In strong form, the unsteady convection-diffusion equation can be written as

$$\begin{aligned} \frac{\partial \varphi}{\partial t} + \boldsymbol{u} \cdot \nabla \varphi - \nabla^2 \varphi = f &\quad \text{in} \quad \Omega, \\ \varphi = 0 &\quad \text{on} \quad \partial\Omega, \\ \varphi = \varphi_0 &\quad \text{at} \quad t = t_0, \end{aligned} \tag{2.1}$$

where $\boldsymbol{u} = [u_x,\, u_y]^T$ is a prescribed two-dimensional velocity field and f is a volumetric heat source. For simplicity, we consider homogeneous Dirichlet boundary conditions with the computational domain given as a rectangle $\Omega = (0, L_x) \times (0, L_y)$.

To derive the weak form, we start by introducing the following function spaces:

$$\begin{aligned} X &= \{v \ \in H^1(\Omega) \mid v = 0 \text{ on } \partial\Omega\} \equiv H^1_0(\Omega), \\ Y(X) &= \{v \mid \forall t \in [0, T], v(x, y; t) \in X, \int_0^T ||v||^2_{H^1(\Omega)} \, \mathrm{d}t < \infty\}. \end{aligned}$$

The weak form is attained by multiplying (2.1) with a test function $v \in X$ and integrating over the domain Ω. By integrating the diffusion term by parts and applying the boundary conditions, we arrive at the following weak problem: find $\varphi \in Y(X)$ such that

$$\int_\Omega \frac{\partial \varphi}{\partial t} v \,\mathrm{d}\Omega + \int_\Omega \nabla\varphi \cdot \nabla v \,\mathrm{d}\Omega + \int_\Omega (\boldsymbol{u} \cdot \nabla\varphi) v \,\mathrm{d}\Omega = \int_\Omega f\, v \,\mathrm{d}\Omega, \quad \forall v \in X.$$

This can also be written as: find $\varphi \in Y(X)$ such that

$$\frac{\mathrm{d}}{\mathrm{d}t}(\varphi, v) + a(\varphi, v) + c(\varphi, v) = (f, v), \quad \forall v \in X, \tag{2.2}$$

where $(\cdot,\cdot)$ denotes a L^2 inner product

$$(u, v) = \int_\Omega u\, v \,\mathrm{d}\Omega,$$

$a(\cdot,\cdot)$ is the symmetric positive-definite (SPD) bilinear form given by

$$a(\varphi, v) = \int_\Omega \nabla\varphi \cdot \nabla v \,\mathrm{d}\Omega,$$

and $c(\cdot,\cdot)$ is the non-symmetric bilinear form defined as

$$c(\varphi, v) = \int_\Omega (\boldsymbol{u} \cdot \nabla\varphi)\, v \,\mathrm{d}\Omega.$$

2.2 Spatial discretization

Throughout this paper we use a Legendre spectral method, i.e. a method based on high-order polynomials. The solution is approximated as high-order polynomials on a reference domain $\widehat{\Omega} = (-1,1)^2$ and transformed onto the physical domain Ω by a mapping $\mathcal{F} : \widehat{\Omega} \longrightarrow \Omega$ (see Figure 2.1). If we denote a point in the reference domain as (ξ, η), then each point (x, y) in the physical domain can uniquely be determined by

$$(x, y) = \mathcal{F}(\xi, \eta).$$

For the rectangular domain we consider here, the mapping is simply a transformation of variables given by

$$x(\xi) = \frac{L_x}{2}(1 + \xi), \tag{2.3}$$

$$y(\eta) = \frac{L_y}{2}(1 + \eta). \tag{2.4}$$

We denote the solution in terms of the reference variables as $\hat{\varphi}(\xi, \eta)$. This can also be written as the composition

$$\hat{\varphi}(\xi, \eta) = \hat{\varphi}(\xi(x), \eta(y)) = (\varphi \circ \mathcal{F})(\xi, \eta) = \varphi(x, y).$$

In the following, we use the hat-notation to indicate that a variable is expressed on the reference domain.

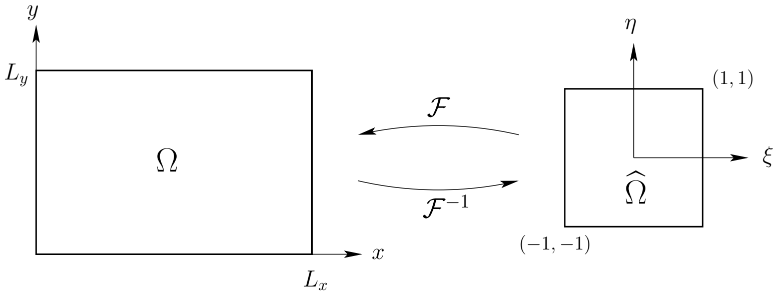

Figure 2.1: The reference domain $\widehat{\Omega}$ mapped to the physical domain Ω.

We now introduce the discrete space X_N defined as

$$X_N = \{v \in H_0^1(\Omega) \mid v \circ \mathcal{F} \in \mathbb{P}_N(\widehat{\Omega})\}.$$

where the notation $v \circ \mathcal{F} \in \mathbb{P}_N(\widehat{\Omega})$ means that v is a polynomial of degree N or less on the reference domain. The high-order polynomial space $\mathbb{P}_N(\widehat{\Omega})$ is defined as the space of functions which are polynomials of degree N or less in each spatial direction:

$$\mathbb{P}_N(\widehat{\Omega}) = \{v(\xi,\eta)\ :\ v(\xi,\eta^*) \in \mathbb{P}_N((-1,1)), v(\xi^*,\eta) \in \mathbb{P}_N((-1,1))\},$$

where the $*$-superscript denotes that the variable value is fixed.

As a basis for the space $\mathbb{P}_N(\widehat{\Omega})$ we use a nodal basis based on a two-dimensional tensor product GLL grid (see Figure 2.2) defined as

$$\forall\, \hat{v} \in \mathbb{P}_N(\widehat{\Omega}), \quad \hat{v}(\xi,\eta) = \sum_{m=0}^{N}\sum_{n=0}^{N} v_{mn}\ell_m(\xi)\ell_n(\eta).$$

Here, $\phi_{mn} = \ell_m(\xi)\ell_n(\eta), 0 \le m,n \le N$, are two-dimensional separable basis functions, where $\ell_n(\xi), \ell_m(\eta)$ are Lagrangian interpolants through the GLL points in each spatial direction. The basis coefficients v_{mn} are represented using a *local* numbering scheme, i.e., each node in the tensor-product GLL grid is represented using two integers (the mth GLL point in the ξ-direction and the nth GLL point in the η-direction).

The Lagrangian interpolants are all polynomials of degree N, and they also have the following important property:

$$\ell_i(\xi_j) = \delta_{ij}, \quad 0 \le i,j \le N, \tag{2.5}$$

where δ_{ij} is the Kronecker delta defined as

$$\delta_{ij} = \begin{cases} 0 \text{ if } i \neq j, \\ 1 \text{ if } i = j. \end{cases}$$

The latter property implies that $\hat{v}(\xi_m,\xi_n) = v_{mn}$, i.e. a nodal basis.

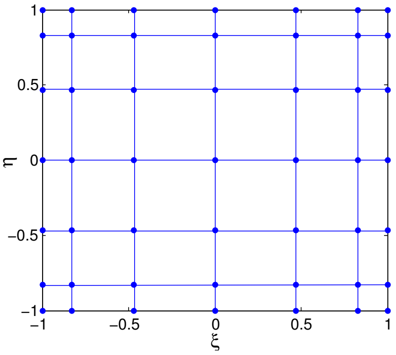

Figure 2.2: The two-dimensional tensor product GLL grid on the reference domain for $N = 6$. The nodes are sited in $(\xi_i, \xi_j), 0 \leq i, j \leq N$.

Having defined a basis for $\mathbb{P}_N(\widehat{\Omega})$, a basis for X_N can be expressed as

$$\hat{\varphi}_N(\xi, \eta) = \sum_{m=1}^{N-1} \sum_{n=1}^{N-1} \varphi_{mn} \ell_m(\xi) \ell_n(\eta).$$

Note that the indices are reduced compared to the basis for $\mathbb{P}_N(\widehat{\Omega})$ due to the homogeneous Dirichlet boundary conditions.

Having defined the discrete space X_N, the discrete problem of (2.2) can now be stated as: find $\varphi_N \in Y(X_N)$ such that

$$\frac{\mathrm{d}}{\mathrm{d}t}(\varphi_N, v) + a(\varphi_N, v) + c(\varphi_N, v) = (f, v), \quad \forall v \in X_N. \tag{2.6}$$

To evaluate the integrals in (2.6), we use a numerical integration method known as Gauss–Lobatto–Legendre (GLL) quadrature (see Appendix A.1). In the following, we denote evaluation by GLL quadrature with a N-subscript, e.g. $(f, v)_N$. Hence, we can state the discrete problem as: find $\varphi_N \in Y(X_N)$ such that

$$\frac{\mathrm{d}}{\mathrm{d}t}(\varphi_N, v)_N + a_N(\varphi_N, v) + c_N(\varphi_N, v) = (f, v)_N, \quad \forall v \in X_N. \tag{2.7}$$

Consider now the evaluation of $(f, v)_N$. By using (2.3)-(2.4), we transform the physical variables into reference variables as follows:

$$\begin{aligned} (f, v)_N &= \int_{\Omega} f\, v \,\mathrm{d}x \,\mathrm{d}y \\ &= \int_{\widehat{\Omega}} \hat{f}\, \hat{v}\, \frac{\mathrm{d}x}{\mathrm{d}\xi} \mathrm{d}\xi\, \frac{\mathrm{d}y}{\mathrm{d}\eta} \mathrm{d}\eta \\ &= \frac{L_x L_y}{4} \int_{\widehat{\Omega}} \hat{f}\, \hat{v} \,\mathrm{d}\xi \,\mathrm{d}\eta. \end{aligned}$$

Choosing the test functions systematically to be the basis functions $\phi_{ij}, 1 \leq i, j \leq N-1$, and by applying GLL quadrature, we obtain

$$\begin{aligned}
\frac{L_x L_y}{4} \int_{\widehat{\Omega}} \hat{f}\, \hat{v}\, \mathrm{d}\xi\, \mathrm{d}\eta &= \frac{L_x L_y}{4} \int_{\widehat{\Omega}} \hat{f}(\xi,\eta)\ell_i(\xi)\ell_j(\eta)\, \mathrm{d}\xi\, \mathrm{d}\eta \\
&\simeq \frac{L_x L_y}{4} \sum_{\alpha=0}^{N} \sum_{\beta=0}^{N} \rho_\alpha \rho_\beta \hat{f}(\xi_\alpha,\xi_\beta)\ell_i(\xi_\alpha)\ell_j(\xi_\beta) \\
&= \frac{L_x L_y}{4} \sum_{\alpha=0}^{N} \sum_{\beta=0}^{N} \rho_\alpha \delta_{i\alpha}\, \rho_\beta \delta_{j\beta}\, \hat{f}(\xi_\alpha,\xi_\beta) \\
&= \frac{L_x L_y}{4} \sum_{\alpha=1}^{N-1} \sum_{\beta=1}^{N-1} B^1_{i\alpha} B^1_{j\beta} f_{\alpha\beta}, \qquad 1 \leq i,j \leq N-1, \qquad (2.8)
\end{aligned}$$

where $\boldsymbol{B}^1$ is the one-dimensional diagonal mass matrix with elements $B^1_{ij} = \rho_i \delta_{ji}$ and $f_{\alpha\beta}$ is the heat source sampled at the physical point $(x(\xi_\alpha), y(\xi_\beta))$. If we represent the sampled values of f in a two-dimensional array $\boldsymbol{F}$, with elements $F_{\alpha\beta} = f_{\alpha\beta}$, we can write (2.8) as

$$(f,v)_N = \frac{L_x L_y}{4} \boldsymbol{B}^1 \boldsymbol{F} (\boldsymbol{B}^1)^T.$$

Hence, we can evaluate the expression locally by two matrix-matrix products, each requiring $\mathcal{O}(N^3)$ floating point operations. Note that we have here not exploited the fact that $\boldsymbol{B}^1$ is diagonal.

However, it is more convenient to express the system of equations if we use a *global* numbering scheme for the field variables. Using global numbering, all the nodes of the two-dimensional GLL grid are represented with a single integer, where the nodes are numbered first in the ξ-direction, then in the η-direction. For instance, we can write the volumetric heat source using a global numbering scheme as

$$\boldsymbol{f} = \begin{bmatrix} f_1 \\ f_2 \\ \vdots \\ \vdots \\ \vdots \\ f_{\mathcal{N}} \end{bmatrix} = \begin{bmatrix} f_{00} \\ f_{10} \\ \vdots \\ f_{ij} \\ \vdots \\ f_{NN} \end{bmatrix},$$

where $\mathcal{N} = (N+1)^2$ is the number of nodes. The relationship between the local and the global representation can be expressed using the tensor product defined in Appendix A.2. Defining $\boldsymbol{f}$ and $\boldsymbol{F}$ as the global and the local representation of the sampled heat source, respectively, we have the following relationship between the two ways of variable

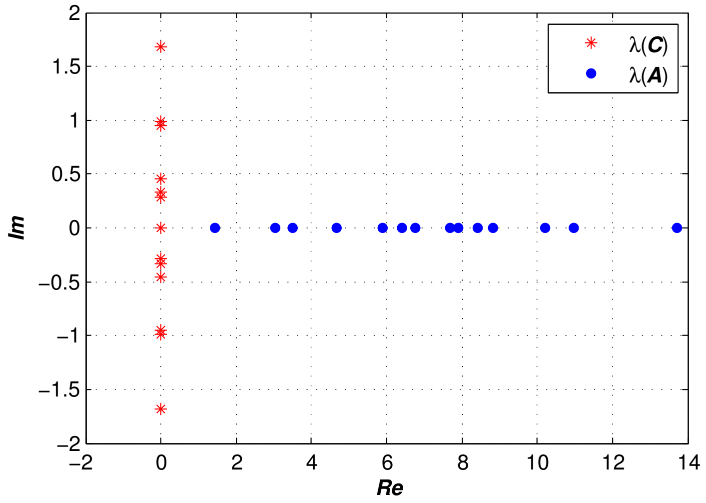

Figure 2.3: Eigenvalues for the two-dimensional discrete diffusion operator and the two-dimensional discrete convection operator for $N = 5$. We see that the eigenvalues are pure real and pure imaginary for the two matrices.

representation [6]

$$\underbrace{(\boldsymbol{B}^1 \otimes \boldsymbol{B}^1)\boldsymbol{f}}_{Global} \leftrightarrow \underbrace{\boldsymbol{B}^1\boldsymbol{F}(\boldsymbol{B}^1)^T}_{Local}.$$

Hence, we can write

$$\frac{L_xL_y}{4}\boldsymbol{B}^1\boldsymbol{F}(\boldsymbol{B}^1)^T \rightarrow \frac{L_xL_y}{4}(\boldsymbol{B}^1 \otimes \boldsymbol{B}^1)\boldsymbol{f} = \boldsymbol{B}\boldsymbol{f},$$

where $\boldsymbol{B}$ is the two-dimensional mass matrix. Using a similar procedure for the rest of the terms is (2.7), we arrive at the semi-discrete (discrete in space, continuous in time) formulation

$$\boldsymbol{B}\,\frac{\mathrm{d}\boldsymbol{\varphi}}{\mathrm{d}t} + \boldsymbol{A}\,\boldsymbol{\varphi} = \boldsymbol{B}\,\boldsymbol{f} - \boldsymbol{C}\,\boldsymbol{\varphi}. \tag{2.9}$$

This is a system of ordinary differential equations where $\boldsymbol{A}$ is the two-dimensional discrete diffusion operator, and $\boldsymbol{C}$ is the two-dimensional discrete convection operator.

2.3 Temporal discretization

In the following we denote a numerical approximation of φ at time t^n as φ^n. By using a fixed time step Δt, we define $t^n = t_0 + n\,\Delta t$.

For the temporal discretization we want to treat each of the operators in (2.9) separately, to better exploit their individual properties. The discrete diffusion operator $\boldsymbol{A}$

is SPD (the eigenvalues of $\boldsymbol{A}$ are depicted in Figure 2.3), favourizing an implicit treatment to avoid time step restrictions. In this case, we use a qth-order backward difference formula (BDFq) given by

$$\frac{\mathrm{d}\varphi^{n+1}}{\mathrm{d}t} \approx \frac{1}{\Delta t}\Big(\beta_q\varphi^{n+1} - \sum_{j=0}^{q-1}\beta_j\varphi^{n-j}\Big),$$

where $\beta_j, j = 0, ..., q$, are given constants. These methods approximate the derivative of a function φ at time t^{n+1} based on the approximate values of φ at a few time steps. To simplify notation we define

$$S\varphi^{n+1} = \beta_q\varphi^{n+1} - \sum_{j=0}^{q-1}\beta_j\varphi^{n-j},$$

giving the following expression for a BDFq approximation

$$\frac{\mathrm{d}\varphi^{n+1}}{\mathrm{d}t} \approx \frac{1}{\Delta t}S\varphi^{n+1}.$$

For instance, the first- and second-order BDFq approximations are given as

$$\begin{aligned} q = 1: \quad & \frac{\mathrm{d}\varphi^{n+1}}{\mathrm{d}t} \approx \frac{1}{\Delta t}\Big(\varphi^{n+1} - \varphi^n\Big), \\ q = 2: \quad & \frac{\mathrm{d}\varphi^{n+1}}{\mathrm{d}t} \approx \frac{1}{\Delta t}\Big(\frac{3}{2}\varphi^{n+1} - 2\varphi^n + \frac{1}{2}\varphi^{n-1}\Big). \end{aligned}$$

The discrete convection operator is not SPD, and has pure imaginary eigenvalues (also depicted in Figure 2.3). In fact, the discrete convection operator is skew-symmetric and we prefer to treat this operator explicitly. Here, we use qth-order extrapolation (EXq) given by

$$\varphi^{n+1} \approx \varphi^{\star,n+1} = \sum_{j=0}^{q-1}\gamma_j\ \varphi^{n-1}.$$

For instance, the first- and second-order EXq approximations are given as

$$\begin{aligned} q = 1: \quad & \varphi^{\star,n+1} = \varphi^n, \\ q = 2: \quad & \varphi^{\star,n+1} = 2\varphi^n - \varphi^{n-1}. \end{aligned}$$

By using the BDFq and the EXq approximations, we can approximate (2.9) as

$$\Big(\boldsymbol{B}\frac{S}{\Delta t} + \boldsymbol{A}\Big)\boldsymbol{\varphi}^{n+1} = \boldsymbol{B}\boldsymbol{f}^{n+1} - (\boldsymbol{C}\boldsymbol{\varphi})^{\star,n+1}.$$

Note that the discrete convection operator is included in the extrapolation, since the convection operator depends on the velocity field which may be dependent of time. For instance, a second-order discretization scheme results in the following set of equations

$$\Big(\boldsymbol{A} + \frac{3}{2\Delta t}\boldsymbol{B}\Big)\boldsymbol{\varphi}^{n+1} = \boldsymbol{B}\boldsymbol{f}^{n+1} + \frac{2}{\Delta t}\boldsymbol{B}\boldsymbol{\varphi}^n - \frac{1}{2\Delta t}\boldsymbol{B}\boldsymbol{\varphi}^{n-1} - 2\boldsymbol{C}^n\boldsymbol{\varphi}^n + \boldsymbol{C}^{n-1}\boldsymbol{\varphi}^{n-1}. \quad (2.10)$$

This is a set of Helmholtz-type equations for the unknown $\boldsymbol{\varphi}^{n+1}$. Due to the positive definiteness of $\boldsymbol{A}$ and $\boldsymbol{B}$, this problem can be solved by the conjugate gradient method. However, there is a way to create a fast direct solver that exploits the simple rectangular geometry of the problem. The method is explained in the next section.

2.4 Tensor product solver for the Helmholtz problem

Let us now consider a Helmholtz system given as

$$(\boldsymbol{A} + \alpha \boldsymbol{B})\boldsymbol{\varphi} = \boldsymbol{g}, \tag{2.11}$$

where $\boldsymbol{A}$ and $\boldsymbol{B}$ are the two-dimensional discrete diffusion operator and the two-dimensional mass matrix, respectively. Note that (2.10) is on the exact same form as (2.11) with $\alpha = \frac{3}{2\Delta t}$ and the right hand side terms collected in the vector $\boldsymbol{g}$.

Using the tensor product, we can write (2.11) as (we assume that $L_x = L_y = 2$)

$$(\underbrace{\boldsymbol{B}^1 \otimes \boldsymbol{A}^1 + \boldsymbol{B}^1 \otimes \boldsymbol{A}^1}_{\boldsymbol{A}} + \alpha \underbrace{(\boldsymbol{B}^1 \otimes \boldsymbol{B}^1)}_{\boldsymbol{B}})\boldsymbol{\varphi} = \boldsymbol{g}, \tag{2.12}$$

where $\boldsymbol{A}^1$ is the one-dimensional discrete diffusion operator.

To solve this system, we start by considering the generalized eigenvalue problem

$$\boldsymbol{A}^1 \boldsymbol{q}_i = \lambda_i \boldsymbol{B}^1 \boldsymbol{q}_i, \quad 1 \leq i \leq N-1,$$

where $\boldsymbol{q}_i$ (assumed to be normalized) represents an eigenvector and λ_i is the corresponding eigenvalue. If we collect the eigenvectors in a matrix $\boldsymbol{Q} = [\boldsymbol{q}_1, ..., \boldsymbol{q}_{N-1}]$ and the eigenvalues in a matrix $\boldsymbol{\Lambda} = \text{diag}(\lambda_1, ..., \lambda_{N-1})$, we can write

$$\boldsymbol{A}^1 \boldsymbol{Q} = \boldsymbol{B}^1 \boldsymbol{Q} \boldsymbol{\Lambda}.$$

Since the eigenvectors should be orthogonal with respect to $\boldsymbol{B}^1$, i.e. $\boldsymbol{Q}^T \boldsymbol{B}^1 \boldsymbol{Q} = \boldsymbol{I}$, we can derive the following expressions for $\boldsymbol{B}^1$ and $\boldsymbol{A}^1$:

$$\begin{aligned}\boldsymbol{B}^1 &= \boldsymbol{Q}^{-T} \boldsymbol{Q}^{-1}, \\ \boldsymbol{A}^1 &= \boldsymbol{Q}^{-T} \boldsymbol{\Lambda} \boldsymbol{Q}^{-1}.\end{aligned}$$

By inserting this into the expression (2.12) and using the properties of the tensor product (see Appendix A.2), we obtain

$$(\boldsymbol{Q}^{-T} \otimes \boldsymbol{Q}^{-T})(\boldsymbol{I} \otimes \boldsymbol{\Lambda} + \boldsymbol{\Lambda} \otimes \boldsymbol{I} + \alpha(\boldsymbol{I} \otimes \boldsymbol{I}))(\boldsymbol{Q}^{-1} \otimes \boldsymbol{Q}^{-1})\boldsymbol{\varphi} = \boldsymbol{g}.$$

By using property **(ii)** of the tensor product, we can write

$$\boldsymbol{\varphi} = (\boldsymbol{Q} \otimes \boldsymbol{Q})(\boldsymbol{I} \otimes \boldsymbol{\Lambda} + \boldsymbol{\Lambda} \otimes \boldsymbol{I} + \alpha(\boldsymbol{I} \otimes \boldsymbol{I}))^{-1}(\boldsymbol{Q}^T \otimes \boldsymbol{Q}^T)\boldsymbol{g}.$$

This product can be divided into three steps:

1. $\boldsymbol{v} = (\boldsymbol{Q}^T \otimes \boldsymbol{Q}^T)\boldsymbol{g}$
2. $\boldsymbol{w} = (\boldsymbol{I} \otimes \boldsymbol{\Lambda} + \boldsymbol{\Lambda} \otimes \boldsymbol{I} + \alpha(\boldsymbol{I} \otimes \boldsymbol{I}))^{-1}\boldsymbol{v}$
3. $\boldsymbol{\varphi} = (\boldsymbol{Q} \otimes \boldsymbol{Q})\boldsymbol{w}$.

To convert back to a local data representation, we use the following relation (for general $\boldsymbol{A}$, $\boldsymbol{B}$ and $\boldsymbol{v}$)

$$\underbrace{(\boldsymbol{A} \otimes \boldsymbol{B})\boldsymbol{v}}_{Global} \leftrightarrow \underbrace{\boldsymbol{B}\ \boldsymbol{V}\ \boldsymbol{A}^T}_{Local}.$$

By using the fact that the tensor product of two diagonal matrices is diagonal in the second step, we can compute the solution in three steps as explained in Algorithm 1. Note that this is a *direct* solver that solves the Helmholtz problem in $\mathcal{O}(N^3)$ operations with only $\mathcal{O}(N^2)$ storage requirement (we only need to store one-dimensional matrices). In comparison, a direct method based on Gaussian elimination would require $\mathcal{O}(N^6)$ floating point operations and $\mathcal{O}(N^4)$ storage requirement.

Algorithm 1 Fast direct Helmholtz solver using tensor products

```
1. $\boldsymbol{V} = \boldsymbol{Q}^T \boldsymbol{G}\, \boldsymbol{Q}$
2.
for $i, j = 1, ..., N - 1$ do
    $W_{ij} = \frac{V_{ij}}{\lambda_i + \lambda_j + \alpha}$
end for
3. $\boldsymbol{\varphi} = \boldsymbol{Q}\ \boldsymbol{W} \boldsymbol{Q}^T$
```

2.5 A numerical example: the convection-diffusion equation

We now solve an unsteady convection-diffusion problem with $\boldsymbol{u} = [1,\, 1]^T$ and the volumetric heat source adjusted such that the exact solution on the domain $\Omega = (0,1) \times (0,1)$ is given by

$$\varphi(x, y, t) = \pi \sin(2\pi y) \sin^2(\pi x) \sin t.$$

Figure 2.4 shows the discretization error at time $T = 1$ for this problem, solved with a second-order temporal discretization scheme (BDF2/EX2). The error is measured in the energy norm and the L^2 norm defined respectively as

$$||v||^2_{E(\Omega)} \equiv a(v, v)$$

and

$$||v||^2_{L^2(\Omega)} \equiv (v, v).$$

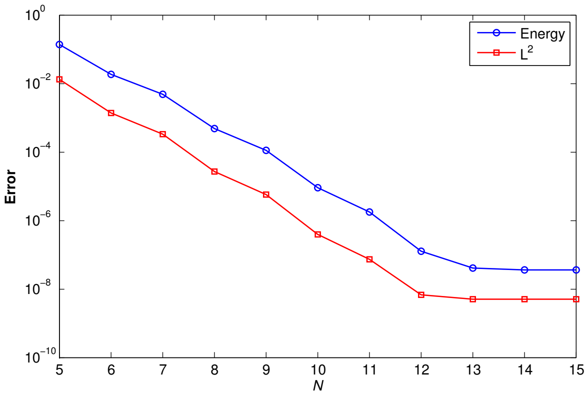

(a)

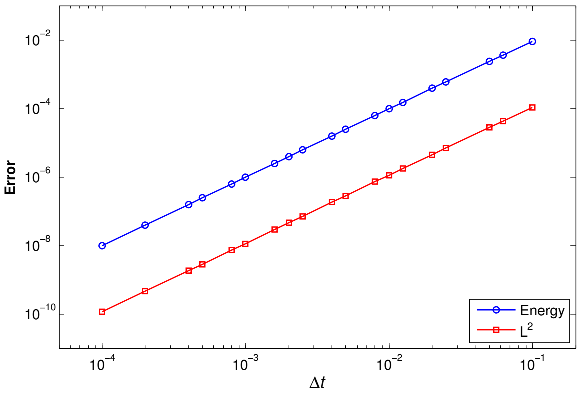

(b)

Figure 2.4: Discretization error at time $T = 1$. In a) we see the error as a function of N for a fixed $\Delta t = 10^{-3}$, making the temporal error subdominant the spatial error for $N \leq 12$. For $N > 12$, the temporal error dominates. We clearly see exponential convergence in space. In b) we see the discretization error as a function of Δt for a fixed $N = 30$, making the spatial error subdominant the temporal error. In this case, we obtain second-order convergence in time, as expected.

In Figure 2.4a we see the error as a function of N for a fixed $\Delta t = 10^{-3}$, in which the temporal error is subdominant the spatial error (for $N \leq 12$). We clearly see exponential convergence, which is expected due to the fact that the domain is rectangular and the exact solution is analytic.

In Figure 2.4b we see the error as a function of Δt for a fixed $N = 30$, in which case the spatial error is subdominant the temporal error. We clearly see second-order convergence in time, as expected.

Chapter 3

Unsteady Stokes flow

In this chapter we take a step towards the Navier–Stokes equations, and consider the incompressible unsteady Stokes equations. These equations represent viscous fluid flow with a low Reynolds number, where the forces due to convection are negligible. This is also known as creeping flows.

3.1 Governing equations

In primitive variables, the governing equations for incompressible unsteady Stokes flow can be written as

$$\rho\frac{\partial \boldsymbol{u}}{\partial t} - \mu\nabla^2\boldsymbol{u} + \nabla p = \boldsymbol{f} \quad \text{in} \quad \Omega, \tag{3.1}$$

$$\nabla\cdot\boldsymbol{u} = 0 \quad \text{in} \quad \Omega, \tag{3.2}$$

$$\boldsymbol{u} = \boldsymbol{0} \quad \text{on} \quad \partial\Omega. \tag{3.3}$$

where $\boldsymbol{u}$ is a two-dimensional velocity field, p is a scalar pressure field and $\boldsymbol{f}$ is a body force. Body forces consist of all forces that are excerted on the fluid without physical contact [7], e.g. the force due to gravity. The constants ρ and μ are the fluids density and dynamic viscosity, respectively, assumed to be $\rho = 1$ and $\mu = 1$.

For the velocity field, we impose no-slip boundary conditions (i.e., $\boldsymbol{u} = \boldsymbol{0}$ on $\partial\Omega$). Here, the domain is given as the rectangle $\Omega = (0, L_x) \times (0, L_y)$. Note that there is no boundary conditions for the pressure.

3.2 Uniqueness

To check for uniqueness, we consider two steady solutions $(\boldsymbol{u}_1, p_1)$ and $(\boldsymbol{u}_2, p_2)$ of the steady Stokes problem ($\frac{\partial}{\partial t} = 0$)

$$\begin{aligned} -\nabla^2\boldsymbol{u} + \nabla p &= \boldsymbol{f} \quad \text{in} \quad \Omega, \\ \nabla\cdot\boldsymbol{u} &= 0 \quad \text{in} \quad \Omega, \\ \boldsymbol{u} &= \boldsymbol{0} \quad \text{on} \quad \partial\Omega. \end{aligned}$$

Due to linearity, $\boldsymbol{w} = \boldsymbol{u}_1 - \boldsymbol{u}_2$ and $q = p_1 - p_2$ represent a solution to the system

$$\begin{aligned} -\nabla^2 \boldsymbol{w} + \nabla q &= 0 \quad \text{in} \quad \Omega, \\ \nabla \cdot \boldsymbol{w} &= 0 \quad \text{in} \quad \Omega, \\ \boldsymbol{w} &= \boldsymbol{0} \quad \text{on} \quad \partial\Omega. \end{aligned}$$

We now multiply the momentum equations with $w_i, i = 1, 2$, and integrate over the domain Ω:

$$-\int_\Omega (\nabla^2 w_i) w_i \, \mathrm{d}\Omega + \int_\Omega \Big(\frac{\partial q}{\partial x_i}\Big) w_i \, \mathrm{d}\Omega = 0, \quad i = 1, 2.$$

Integrating by parts and applying the boundary conditions ($\boldsymbol{w} = \boldsymbol{0}$ on $\partial\Omega$), we get

$$\int_\Omega \nabla w_i \cdot \nabla w_i \, \mathrm{d}\Omega - \int_\Omega q \cdot \frac{\partial w_i}{\partial x_i} \, \mathrm{d}\Omega = 0, \quad i = 1, 2.$$

By adding the momentum equations, we arrive at

$$\int_\Omega (|\nabla w_1|^2 + |\nabla w_2|^2) \, \mathrm{d}\Omega - \int_\Omega q \underbrace{\nabla \cdot \boldsymbol{w}}_{=0 \text{ in } \Omega} \, \mathrm{d}\Omega = 0.$$

Hence,

$$\begin{aligned} \nabla w_i &= 0 \quad \text{in } \Omega, \quad i = 1, 2, \\ \implies w_i &= 0 \quad \text{in } \Omega, \quad i = 1, 2, \\ \implies \boldsymbol{u}_1 &= \boldsymbol{u}_2 \quad \text{in } \Omega, \end{aligned}$$

proving the uniqueness of the velocity field.

Having proved that $\boldsymbol{w} = \boldsymbol{0}$ in Ω, it follows from the momentum equations that $\nabla q = 0$, which in turn implies that q is constant in Ω. As a result of this, we can only determine the pressure up to a constant, i.e., if p_1 is a solution, so is

$$p_2 = p_1 + p_0,$$

where p_0 is a constant known as the hydrostatic mode.

3.3 Splitting scheme

To solve (3.1)–(3.3) numerically, we apply an operator splitting scheme introduced in [1]. The key idea behind this particular splitting scheme is to find the pressure by testing the momentum equations against gradients, i.e., we want to find $p \in Y = H^1(\Omega)$ such that

$$\int_\Omega \Big(\frac{\partial \boldsymbol{u}}{\partial t} - \nabla^2 \boldsymbol{u} + \nabla p\Big) \cdot \nabla q \; \mathrm{d}\Omega = \int_\Omega \boldsymbol{f} \cdot \nabla q \; \mathrm{d}\Omega, \quad \forall q \in Y.$$

Using Gauss's theorem and the divergence constraint for the velocity field, we can show that the time-dependent term vanish for the present boundary conditions:

$$\begin{aligned}\int_\Omega \frac{\partial \boldsymbol{u}}{\partial t} \cdot \nabla q \ \mathrm{d}\Omega &= \int_\Omega \nabla \cdot \Big(\frac{\partial \boldsymbol{u}}{\partial t} q\Big) \ \mathrm{d}\Omega - \int_\Omega q \nabla \cdot \frac{\partial \boldsymbol{u}}{\partial t} \ \mathrm{d}\Omega \\ &= \underbrace{\int_{\partial\Omega} \Big(\frac{\partial \boldsymbol{u}}{\partial t} q\Big) \cdot \boldsymbol{n} \ \mathrm{d}s}_{\boldsymbol{u}|_{\partial\Omega}=0} - \int_\Omega q \frac{\partial}{\partial t} \underbrace{\nabla \cdot \boldsymbol{u}}_{=0} \ \mathrm{d}\Omega = 0.\end{aligned}$$

Hence, we are left with the following problem: find $p \in Y = H^1(\Omega)$ such that

$$\int_\Omega \nabla p \cdot \nabla q \ \mathrm{d}\Omega = \int_\Omega \Big(\boldsymbol{f} + \nabla^2 \boldsymbol{u}\Big) \cdot \nabla q \ \mathrm{d}\Omega, \quad \forall q \in Y.$$

It turns out that the accuracy of the splitting scheme can be improved if the term $\nabla^2 \boldsymbol{u}$ is replaced by $-\nabla \times \nabla \times \boldsymbol{u}$ using the identity

$$\nabla^2 \boldsymbol{u} = \nabla \underbrace{\nabla \cdot \boldsymbol{u}}_{=0} - \nabla \times \nabla \times \boldsymbol{u} \implies \nabla^2 \boldsymbol{u} = -\nabla \times \nabla \times \boldsymbol{u}.$$

Inserting this into the pressure equation then yields the following weak problem for the pressure: find $p \in Y = H^1(\Omega)$ such that

$$\int_\Omega \nabla p \cdot \nabla q \ \mathrm{d}\Omega = \int_\Omega (\boldsymbol{f} - \nabla \times \nabla \times \boldsymbol{u}) \cdot \nabla q \ \mathrm{d}\Omega, \quad \forall q \in Y.$$

This may also be written as: find $p \in Y = H^1(\Omega)$ such that

$$a(p, q) = (\boldsymbol{f} - \nabla \times \nabla \times \boldsymbol{u}, \nabla q), \quad \forall q \in Y, \tag{3.4}$$

where we remind that $a(\cdot, \cdot)$ and $(\cdot, \cdot)$ are given by

$$\begin{aligned} a(w, v) &= \int_\Omega \nabla w \cdot \nabla v \, \mathrm{d}\Omega, \\ (w, v) &= \int_\Omega w \, v \, \mathrm{d}\Omega. \end{aligned}$$

Note that if the velocity field $\boldsymbol{u}$ is known, (3.4) is simply a weak Poisson problem for the pressure with pure homogeneous Neumann boundary conditions.

When solving for the velocity field, our point of departure is the weak formulation of the momentum equations. Having pure homogeneous Dirichlet boundary conditions for the velocity, we define the corresponding search space $X = H_0^1(\Omega) \times H_0^1(\Omega) = (H_0^1(\Omega))^2$. The weak form is then attained by multiplying the momentum equations with a test function $\boldsymbol{v} \in X$ and integrate over the domain Ω. Integrating both the diffusion term and the pressure term by parts and applying the boundary conditions, we get the following weak problem for the velocity field: find $\boldsymbol{u} \in X = (H_0^1(\Omega))^2$ such that

$$\int_\Omega \frac{\partial \boldsymbol{u}}{\partial t} \cdot \boldsymbol{v} \ \mathrm{d}\Omega + \int_\Omega \nabla \boldsymbol{u} \cdot \nabla \boldsymbol{v} \ \mathrm{d}\Omega - \int_\Omega p \nabla \cdot \boldsymbol{v} \ \mathrm{d}\Omega = \int_\Omega \boldsymbol{f} \cdot \boldsymbol{v} \ \mathrm{d}\Omega, \quad \forall \boldsymbol{v} \in X. \tag{3.5}$$

Note that we now have a vector of two test functions associated with each spatial grid point. Similarly, the velocity $\boldsymbol{u}$ and the body force $\boldsymbol{f}$ are two-dimensional vectors. Hence, this particular weak problem results into two sets of algebraic equations, one for each velocity component.

Using a shorter notation, we can state (3.5) as: find $\boldsymbol{u} \in X = (H_0^1(\Omega))^2$ such that

$$\frac{\mathrm{d}}{\mathrm{d}t}(\boldsymbol{u}, \boldsymbol{v}) + \boldsymbol{a}(\boldsymbol{u}, \boldsymbol{v}) - \boldsymbol{d}(p, \boldsymbol{v}) = (\boldsymbol{f}, \boldsymbol{v}), \quad \forall \boldsymbol{v} \in X,$$

where $\boldsymbol{d}(\cdot, \cdot)$ is a vector valued bilinear form defined as

$$\boldsymbol{d}(p, \boldsymbol{v}) = \begin{bmatrix} d(p, v_x) = \int_\Omega p \, \frac{\partial v_x}{\partial x} \, \mathrm{d}\Omega \\ d(p, v_y) = \int_\Omega p \, \frac{\partial v_y}{\partial y} \, \mathrm{d}\Omega \end{bmatrix}.$$

Similarly, the L^2 norm and $\boldsymbol{a}(\cdot, \cdot)$ are now vector valued and given as

$$(\boldsymbol{f}, \boldsymbol{v}) = \begin{bmatrix} (f_x, v_x) \\ (f_y, v_y) \end{bmatrix}$$

and

$$\boldsymbol{a}(\boldsymbol{u}, \boldsymbol{v}) = \begin{bmatrix} a(u_x, v_x) \\ a(u_y, v_y) \end{bmatrix}.$$

To summarize, the strong form of the Stokes problem (3.1)–(3.3) has an equivalent weak formulation given by: find $\boldsymbol{u} \in X$ and $p \in Y$ such that

$$1. \quad \frac{\partial}{\partial t}(\boldsymbol{u}, \boldsymbol{v}) + \boldsymbol{a}(\boldsymbol{u}, \boldsymbol{v}) - \boldsymbol{d}(p, \boldsymbol{v}) = (\boldsymbol{f}, \boldsymbol{v}), \quad \forall \boldsymbol{v} \in X. \tag{3.6}$$

$$2. \quad a(p, q) = (\boldsymbol{f} - \nabla \times \nabla \times \boldsymbol{u}, \nabla q), \quad \forall q \in Y. \tag{3.7}$$

Note that these equations constitute a coupled problem in $\boldsymbol{u}$ and p. We also remark that we have stated the equations in an alternative form compared to (3.1)–(3.3). By applying the relation $\nabla^2 \boldsymbol{u} = -\nabla \times \nabla \times \boldsymbol{u}$, we are actually considering a rotational form in (3.7).

The equations (3.6)-(3.7) will be the point of departure for the spatial and the temporal discretizations. The idea of the splitting scheme is to compute the velocity and pressure at each time step in two consecutive steps: first the velocity field is computed from (3.6) by treating the pressure as a known quantity through extrapolation. We then update the pressure from (3.7) by inserting the calculated velocity field.

3.4 Discretization

Let $X_N \subset X$ and $Y_N \subset Y$ be discrete approximation spaces for the velocity and the pressure, respectively. We will soon define X_N and Y_N, but before we do that we mention a general condition for the pressure of the discrete problem to be uniquely defined. In general, a compatibility condition known as the *inf-sup condition* has to be satisfied by the discrete spaces for stability and uniqueness of the discrete solution [11]. The inf-sup condition is given by

$$\inf_{q \in Y_N} \sup_{\boldsymbol{v} \in X_N} \frac{d(q, \boldsymbol{v})}{||\nabla \boldsymbol{v}||_{L^2(\Omega)} ||q||_{L^2(\Omega)}} = \beta_N > 0.$$

If this condition is not satisfied, the space of *spurious pressure modes*

$$Z_N = \{q \in Y_N \mid d(q, \boldsymbol{v}) = 0, \forall \boldsymbol{v} \in X_N\}$$

is not empty. Hence, a solution $p_N^* = p_N + p_s$ is a discrete pressure solution for any $p_s \in Z_N$, implying a non-unique pressure.

In general, to avoid spurious pressure modes, the approximation spaces X_N and Y_N need to be of different order. One appropriate choice of spaces is the $\mathbb{P}_N - \mathbb{P}_{N-2}-$method, where each component of the velocity is approximated with a Nth order polynomial basis, while the pressure is approximated with a polynomial basis of degree $N-2$.

However, it turns out that for the splitting scheme we consider here, the inf-sup condition is not required [1]. This means that the system is well-posed even if the spaces X_N and Y_N are of the same order, and we are free to choose polynomial bases of degree N for both spaces. Hence, we define the discrete spaces X_N and Y_N as

$$\begin{aligned} X_N &= \{\boldsymbol{v} \in X \mid \boldsymbol{v} \circ \mathcal{F} \in (\mathbb{P}_N(\widehat{\Omega}))^2\}, \\ Y_N &= \{q \in Y \mid q \circ \mathcal{F} \in \mathbb{P}_N(\widehat{\Omega})\}. \end{aligned}$$

The discrete problem can now be stated as: find $\boldsymbol{u}_N \in X_N$ and $p_N \in Y_N$ such that

1. $\dfrac{\partial}{\partial t}(\boldsymbol{u}_N, \boldsymbol{v})_N + \boldsymbol{a}_N(\boldsymbol{u}_N, \boldsymbol{v}) - \boldsymbol{d}_N(p_N, \boldsymbol{v}) = (\boldsymbol{f}, \boldsymbol{v})_N, \quad \forall \boldsymbol{v} \in X_N.$

2. $a_N(p_N, q) = (\boldsymbol{f} - \nabla \times \nabla \times \boldsymbol{u}_N, \nabla q)_N, \quad \forall q \in Y_N.$

As basis for the discrete spaces, we use the nodal basis based on the two-dimensional tensor product GLL grid described in Section 2.2. Applying GLL quadrature to evaluate the integrals, we arrive at the following semi-discrete formulation:

$$\begin{aligned} &\left(\boldsymbol{B}\frac{\mathrm{d}}{\mathrm{d}t} + \boldsymbol{A}\right)\boldsymbol{u}_x - \boldsymbol{D}_x\boldsymbol{p} = \boldsymbol{B}\boldsymbol{f}_x, \\ &\left(\boldsymbol{B}\frac{\mathrm{d}}{\mathrm{d}t} + \boldsymbol{A}\right)\boldsymbol{u}_y - \boldsymbol{D}_y\boldsymbol{p} = \boldsymbol{B}\boldsymbol{f}_y, \\ &\boldsymbol{A}\boldsymbol{p} = \boldsymbol{h}. \end{aligned}$$

Here, $\boldsymbol{h}$ is the evaluation of the term $(\boldsymbol{f} - \nabla \times \nabla \times \boldsymbol{u}_N, \nabla q)_N$. Note that the system of equations constitute a coupled problem in the basis coefficients $\boldsymbol{u}_x$, $\boldsymbol{u}_y$ and $\boldsymbol{p}$.

In order to make the pressure explicit for the equations involving the velocity, we approximate the pressure by the EXq method (see Section 2.3). By approximating the time-derivative term by BDFq (again, see Section 2.3), we end up with the following system of algebraic equations [1]:

$$\boldsymbol{B}\Big(\frac{S\boldsymbol{u}_x^{n+1}}{\Delta t}\Big) + \boldsymbol{A}\,\boldsymbol{u}_x^{n+1} - \boldsymbol{D}_x\boldsymbol{p}^{\star,n+1} = \boldsymbol{B}\boldsymbol{f}_x^{n+1}, \tag{3.8}$$

$$\boldsymbol{B}\Big(\frac{S\boldsymbol{u}_y^{n+1}}{\Delta t}\Big) + \boldsymbol{A}\,\boldsymbol{u}_y^{n+1} - \boldsymbol{D}_y\boldsymbol{p}^{\star,n+1} = \boldsymbol{B}\boldsymbol{f}_y^{n+1}, \tag{3.9}$$

$$\boldsymbol{A}\boldsymbol{p}^{n+1} = \boldsymbol{h}^{n+1}, \tag{3.10}$$

where $\boldsymbol{h}^{n+1}$ denotes evaluation of the term $(\boldsymbol{f}^{n+1} - \nabla\times\nabla\times\boldsymbol{u}_N^{n+1}, \nabla q)_N$. Recall that the BDF$q$ and the EXq approximations for $q = 1, 2$ are given as

$$q = 1: \quad S\boldsymbol{u}^{n+1} = \boldsymbol{u}^{n+1} - \boldsymbol{u}^n, \qquad \boldsymbol{p}^{\star,n+1} = \boldsymbol{p}^n.$$

$$q = 2: \quad S\boldsymbol{u}^{n+1} = \frac{3}{2}\boldsymbol{u}^{n+1} - 2\boldsymbol{u}^n + \frac{1}{2}\boldsymbol{u}^{n-1}, \qquad \boldsymbol{p}^{\star,n+1} = 2\boldsymbol{p}^n - \boldsymbol{p}^{n-1}.$$

To solve (3.8)-(3.10), we need to consider the equations in a sequential order for each time step. First, the equations (3.8) and (3.9) are solved for each of the velocity components. Since both equations are of Helmholtz-type, we apply the Helmholtz solver based on tensor product properties (see Algorithm 1 in Section 2.4) to solve the equations.

Second, we use the updated velocity field to compute the right hand side of (3.10), resulting in a set of Poisson equations for the pressure. To update the pressure, we solve the Poisson equation with the same framework as for the Helmholtz solver. Actually, the only difference in the procedure is to set $\alpha = 0$ in step 2 of Algorithm 1.

3.5 A numerical example: unsteady Stokes flow

Let us now test the splitting scheme approximation described in the previous section on the following problem: we adjust the body force $\boldsymbol{f}$ in (3.1) such that the exact solution of (3.1)–(3.3) on the domain $\Omega = (0,1)\times(0,1)$ is given by

$$p(x,y,t) = \cos(\pi x)\sin(\pi y)\sin t, \tag{3.11}$$

$$\boldsymbol{u}(x,y,t) = [\pi\sin(2\pi y)\sin^2(\pi x)\sin t, -\pi\sin(2\pi x)\sin^2(\pi y)\sin t]^T. \tag{3.12}$$

The numerical solution is depicted in Figure 3.1 for $N = 30$. The figure shows the velocity field and the pressure field at time $T = 1$, using a second-order temporal discretization scheme.

In Figure 3.2 we see the discretization error for both the pressure and the velocity using both a first-order and a second-order temporal discretization scheme. Here, the error is as a function of Δt for a fixed $N = 30$, making the spatial error subdominant the temporal error. The error in the velocity is measured in the the energy norm, while the error in the pressure is measured in the L^2 norm. Note that the energy norm now is given by

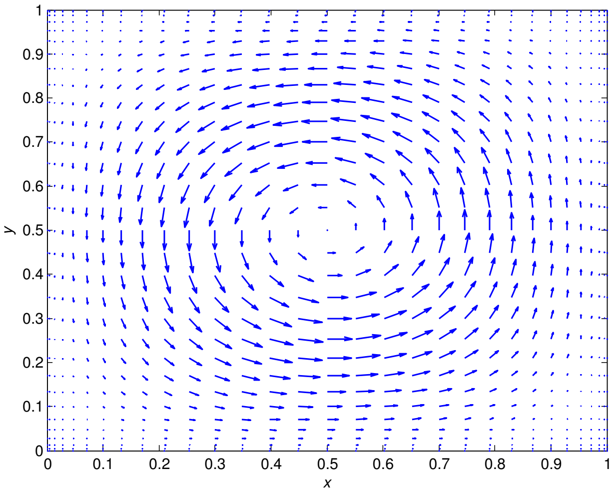

(a)

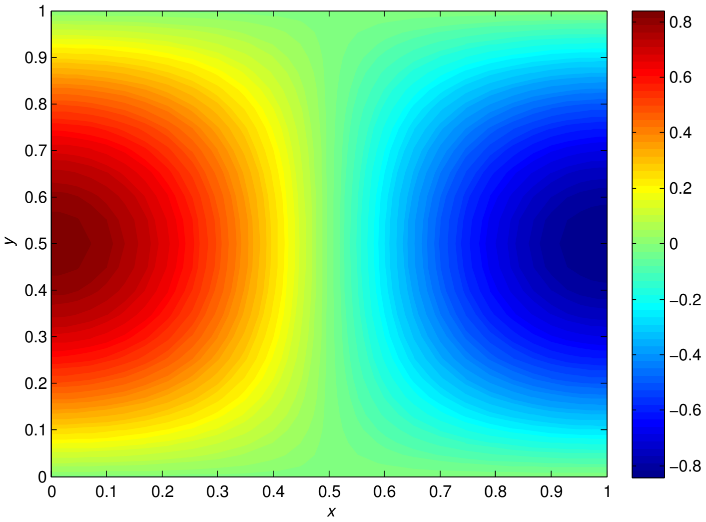

(b)

Figure 3.1: Numerical solution of the test problem with exact solution given by (3.11)-(3.12) for $N = 30$ at time $T = 1$. In a) we see the velocity, while the pressure field is showed in b).

$$||\boldsymbol{v}||^2_{E(\Omega)} = \boldsymbol{a}(\boldsymbol{v},\boldsymbol{v}),$$

where the right hand side is the sum of the contribution from the two integrals of $\boldsymbol{a}(\cdot,\cdot)$. From the figure we clearly see first- and second-order convergence for the first- and second-order temporal discretization schemes, as expected.

In Figure 3.3 we see the discretization error for the velocity measured in the energy norm as a function of N for various fixed Δt. In this case the temporal error is subdominant the spatial error, and we see exponential convergence in space. This is as expected since the domain is a rectangle and the exact solution is analytic. Note that when the time step Δt is reduced by a factor of two, the error is dropping twice as much for the second-order scheme compared to the first-order scheme.

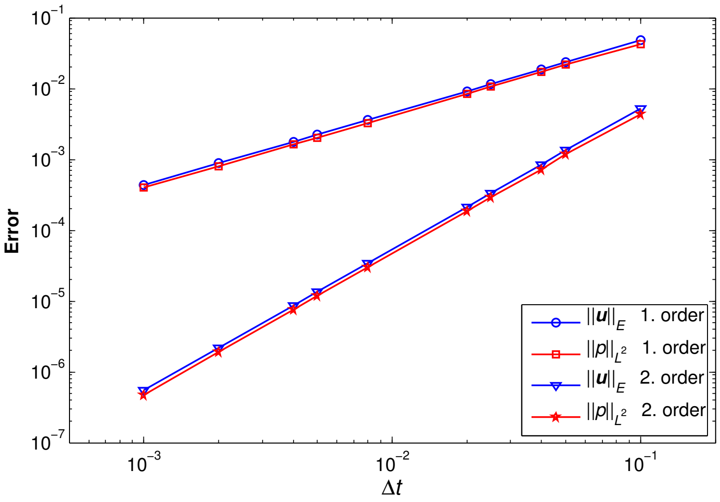

Figure 3.2: Discretization error as a function of Δt for a fixed $N = 30$, making the spatial error subdominant the temporal error. The error of the velocity is measured in the energy norm, while the error in the pressure is measured in the L^2 norm. We clearly see the expected convergence rates for the temporal discretization schemes.

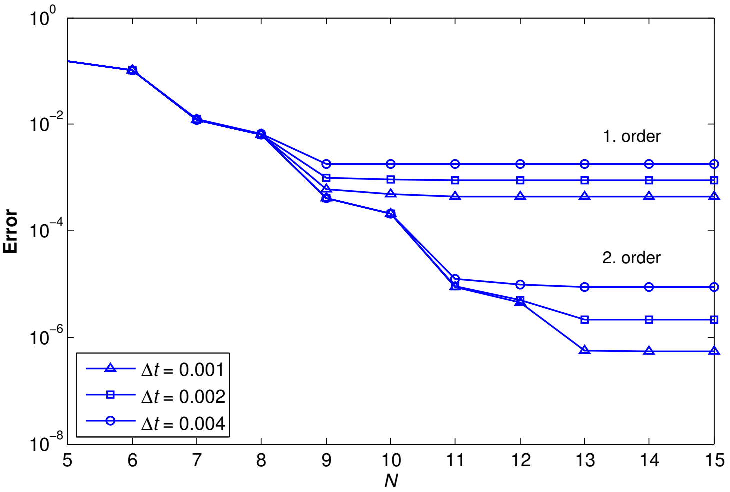

Figure 3.3: Discretization error for the velocity measured in the energy norm as a function of N for various fixed Δt. The three upper graphs show the error for a first-order scheme, while the three lower graphs show the error for a second-order scheme. For the first-order scheme, the temporal error is subdominant the spatial error for $N \leq 8$, while for the second-order scheme, the temporal error is subdominant for $N \leq 11$. If we are in the regime where the temporal error is dominant, and we reduce the time step with a factor of two, we see that the error is reduced by a factor of two for a first-order scheme, and a factor of four for a second-order scheme.

Chapter 4

The Navier–Stokes equations

We now turn the attention to the famous Navier–Stokes (N-S) equations. These equations describe the motion of fluid substances, and are based on the laws of continuum mechanics: conservation of mass and linear momentum [12]. We will here consider incompressible flow for Newtonian fluids, where the stress-strain relationship is linear, making the viscosity constant.

4.1 Governing equations

In primitive variables, the strong form of the incompressible unsteady Navier–Stokes equations can be written as

$$\begin{aligned} \rho\frac{\partial \boldsymbol{u}}{\partial t} + \rho\, \boldsymbol{u}\cdot\nabla\boldsymbol{u} - \mu\nabla^2\boldsymbol{u} + \nabla p = \rho\boldsymbol{f} \quad &\text{in} \quad \Omega, \\ \nabla\cdot\boldsymbol{u} = 0 \quad &\text{in} \quad \Omega, \\ \boldsymbol{u} = \boldsymbol{0} \quad &\text{on} \quad \partial\Omega, \end{aligned}$$

where we again assume no-slip conditions at the boundaries of the rectangular domain $\Omega = (0, L_x) \times (0, L_y)$. The equations can also be written as

$$\frac{\partial \boldsymbol{u}}{\partial t} + \boldsymbol{u}\cdot\nabla\boldsymbol{u} - \nu\nabla^2\boldsymbol{u} + \frac{1}{\rho}\nabla p = \boldsymbol{f} \quad \text{in} \quad \Omega, \tag{4.1}$$

$$\nabla\cdot\boldsymbol{u} = 0 \quad \text{in} \quad \Omega, \tag{4.2}$$

$$\boldsymbol{u} = \boldsymbol{0} \quad \text{on} \quad \partial\Omega, \tag{4.3}$$

where ν is the fluids kinematic viscosity defined as the ratio of the dynamic viscosity and the density.

4.2 Splitting scheme and discretization

There are many ways to solve the N-S equations by using a splitting scheme [23, 24]. Here, we use an extension of the splitting scheme introduced for the Stokes problem.

The challenge of solving the N-S equations compared to the Stokes problem, is the non-linear convection term

$$\boldsymbol{u}\cdot\nabla\boldsymbol{u} = \begin{bmatrix}\boldsymbol{u}\cdot\nabla u_x\\ \boldsymbol{u}\cdot\nabla u_y\end{bmatrix}.$$

Usually, the convection term makes the numerical treatment of the full N-S equations fairly complicated. However, using the splitting scheme idea already introduced, the solution of the equations is surprisingly simple.

Using the same approach as for the Stokes problem, we end up with the following weak problem for the velocity and the pressure, assuming $\nu = 1$ and $\rho = 1$: find $u \in X$ and $p \in Y$ such that

1. $\dfrac{\mathrm{d}}{\mathrm{d}t}(\boldsymbol{u},\boldsymbol{v}) + \boldsymbol{a}(\boldsymbol{u},\boldsymbol{v}) - \boldsymbol{d}(p,\boldsymbol{v}) = (\boldsymbol{f},\boldsymbol{v}) - \boldsymbol{c}(\boldsymbol{u},\boldsymbol{v}), \quad \forall\boldsymbol{v}\in X.$

2. $a(p,q) = (\boldsymbol{f} - \nabla\times\nabla\times\boldsymbol{u},\nabla q) - (\boldsymbol{u}\cdot\nabla\boldsymbol{u},\nabla q), \quad \forall q\in Y.$

Recall that $\boldsymbol{c}(\cdot,\cdot)$ is given by

$$\boldsymbol{c}(\boldsymbol{u},\boldsymbol{v}) = \begin{bmatrix} c(u_x,v_x) = \int_\Omega(\boldsymbol{u}\cdot\nabla u_x)v_x\,\mathrm{d}\Omega\\ c(u_y,v_y) = \int_\Omega(\boldsymbol{u}\cdot\nabla u_y)v_y\,\mathrm{d}\Omega\end{bmatrix}.$$

For the discrete spaces X_N and Y_N we use the same approximation spaces as for the Stokes problem, i.e.

$$\begin{aligned} X_N &= \{\boldsymbol{v}\in X \mid \boldsymbol{v}\circ\mathcal{F}\in(\mathbb{P}_N(\widehat{\Omega}))^2\},\\ Y_N &= \{q\in Y \mid q\circ\mathcal{F}\in\mathbb{P}_N(\widehat{\Omega})\}.\end{aligned}$$

Hence, the discrete problem can be stated as: find $\boldsymbol{u}_N\in X_N$ and $p_N\in Y_N$ such that

1. $\dfrac{\mathrm{d}}{\mathrm{d}t}(\boldsymbol{u}_N,\boldsymbol{v})_N + \boldsymbol{a}_N(\boldsymbol{u}_N,\boldsymbol{v}) - \boldsymbol{d}_N(p_N,\boldsymbol{v}) = (\boldsymbol{f},\boldsymbol{v})_N - \boldsymbol{c}_N(\boldsymbol{u}_N,\boldsymbol{v}), \quad \forall\boldsymbol{v}\in X_N.$

2. $a_N(p_N,q) = (\boldsymbol{f} - \nabla\times\nabla\times\boldsymbol{u}_N,\nabla q)_N - (\boldsymbol{u}_N\cdot\nabla\boldsymbol{u}_N,\nabla q)_N, \quad \forall q\in Y_N.$

Again, the spatial discretization is done by applying the Legendre spectral method, i.e., we use the nodal basis based on the two-dimensional tensor-product GLL grid. Evaluating the integrals by GLL quadrature, we arrive at the following semi-discrete system:

$$\left(\boldsymbol{B}\frac{\mathrm{d}}{\mathrm{d}t} + \boldsymbol{A}\right)\boldsymbol{u}_x - \boldsymbol{D}_x\boldsymbol{p} = \boldsymbol{B}\boldsymbol{f}_x - \boldsymbol{C}\boldsymbol{u}_x, \tag{4.4}$$

$$\left(\boldsymbol{B}\frac{\mathrm{d}}{\mathrm{d}t} + \boldsymbol{A}\right)\boldsymbol{u}_y - \boldsymbol{D}_y\boldsymbol{p} = \boldsymbol{B}\boldsymbol{f}_y - \boldsymbol{C}\boldsymbol{u}_y, \tag{4.5}$$

$$\boldsymbol{A}\boldsymbol{p} = \boldsymbol{h} - \boldsymbol{z}, \tag{4.6}$$

where $\boldsymbol{h} = (\boldsymbol{f} - \nabla \times \nabla \times \boldsymbol{u}_N, \nabla q)_N$ and $\boldsymbol{z} = (\boldsymbol{u}_N \cdot \nabla \boldsymbol{u}_N, \nabla q)_N$. Similar to the Stokes problem, this is a coupled problem in the basis coefficients $\boldsymbol{u}_x$, $\boldsymbol{u}_y$ and $\boldsymbol{p}$.

As we did for the convection-diffusion equation, we use EXq to approximate the convection term at each time step. Note that the evaluation of $\boldsymbol{z}$ is dependent on the convection term, so this term also needs to be extrapolated. Using BDFq for the derivative term, and extrapolating the pressure in the velocity equations, we can approximate (4.4)-(4.6) as [1]:

$$\Big(\boldsymbol{B}\frac{S}{\Delta t} + \boldsymbol{A}\Big)\boldsymbol{u}_x^{n+1} - \boldsymbol{D}_x\boldsymbol{p}^{\star,n+1} = \boldsymbol{B}\boldsymbol{f}_x^{n+1} - (\boldsymbol{C}\boldsymbol{u}_x)^{\star,n+1}, \tag{4.7}$$

$$\Big(\boldsymbol{B}\frac{S}{\Delta t} + \boldsymbol{A}\Big)\boldsymbol{u}_y^{n+1} - \boldsymbol{D}_y\boldsymbol{p}^{\star,n+1} = \boldsymbol{B}\boldsymbol{f}_y^{n+1} - (\boldsymbol{C}\boldsymbol{u}_y)^{\star,n+1}, \tag{4.8}$$

$$\boldsymbol{A}\boldsymbol{p}^{n+1} = \boldsymbol{h}^{n+1} - \boldsymbol{z}^{\star,n+1}, \tag{4.9}$$

where $\boldsymbol{h}^{n+1}$ denotes evaluation of $(\boldsymbol{f}^{n+1} - \nabla \times \nabla \times \boldsymbol{u}_N^{n+1}, \nabla q)_N$, while the extrapolated terms are given as (we only consider second-order)

$$\begin{aligned}
\boldsymbol{z}^{\star,n+1} &= 2 \cdot (\boldsymbol{u}_N^n \cdot \nabla \boldsymbol{u}_N^n, \nabla q)_N - (\boldsymbol{u}_N^{n-1} \cdot \nabla \boldsymbol{u}_N^{n-1}, \nabla q)_N, \\
(\boldsymbol{C}\boldsymbol{u})^{\star,n+1} &= 2 \cdot (\boldsymbol{C}^n\boldsymbol{u}^n) - \boldsymbol{C}^{n-1}\boldsymbol{u}^{n-1}, \\
\boldsymbol{p}^{\star,n+1} &= 2\boldsymbol{p}^n - \boldsymbol{p}^{n-1}.
\end{aligned}$$

Similar to the unsteady Stokes problem, we need to solve two Helmholtz problems for the velocity and one Poisson problem for the pressure at each time step: first we solve (4.7)-(4.8) for each of the velocity components, then we solve (4.9) for the pressure, where the right hand side is evaluated by using the updated velocity.

4.3 A numerical example: the Navier-Stokes equations

In order to test the splitting scheme derived in the previous section, we consider the following test problem: we adjust $\boldsymbol{f}$ in (4.1) such that the exact solution of (4.1)-(4.3) is given as

$$\begin{aligned}
p(x, y, t) &= \cos(\pi x)\sin(\pi y)\sin t, \\
\boldsymbol{u}(x, y, t) &= [\pi \sin(2\pi y)\sin^2(\pi x)\sin t, -\pi \sin(2\pi x)\sin^2(\pi y)\sin t]^T.
\end{aligned}$$

The problem is solved with a second-order discretization scheme. Note that the exact solution is similar to the test problem of the Stokes problem.

In Figure 4.1 we see the discretization error as a function of Δt for a fixed $N = 30$, in which case the spatial error is subdominant the temporal error. Here, the error in the velocity is measured in the energy norm, while the error in the pressure is measured in the L^2 norm. We clearly see second-order convergence in time, as expected.

In Figure 4.2 we see the discretization error as a function of N for a fixed $\Delta t = 10^{-3}$, in which the temporal error is subdominant the spatial error (for $N \leq 12$). Again, the error in the velocity is measured in the energy norm, while the error in the pressure is measured in the L^2 norm. We clearly see exponential convergence, which is expected due to the fact that the domain is rectangular and the exact solution is analytic.

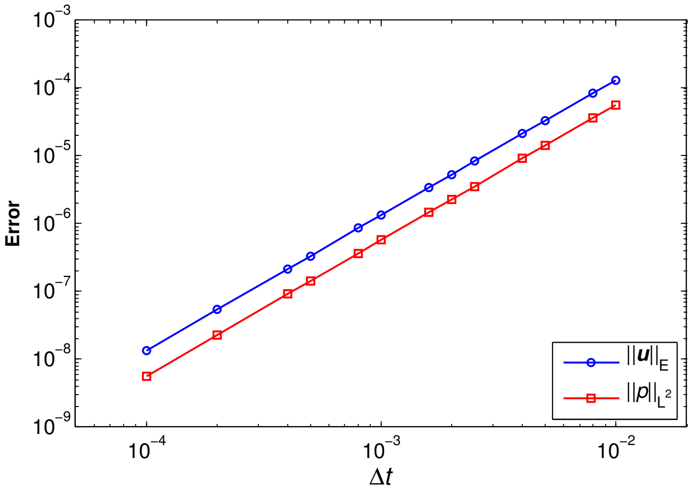

Figure 4.1: Discretization error at time $T = 1$ as a function of Δt for a fixed $N = 30$, making the spatial error subdominant the temporal error. The error in the velocity is measured in the energy norm, while the error in the pressure is measured in the L^2 norm. We clearly see second-order convergence in time, as expected.

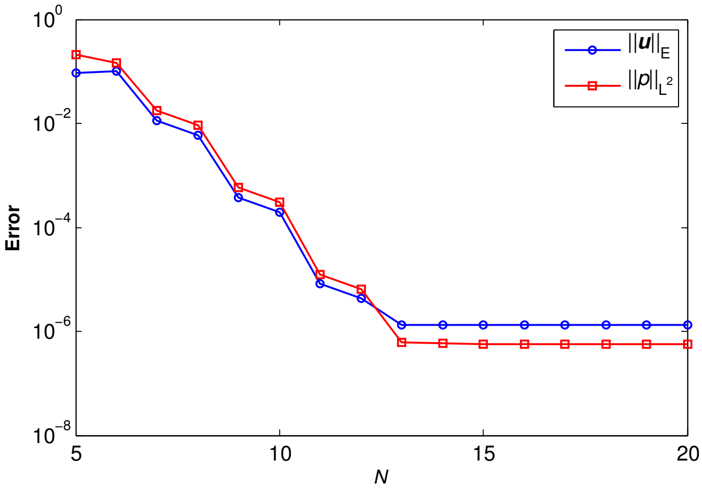

Figure 4.2: Discretization error at time $T = 1$ as a function of N for a fixed $\Delta t = 10^{-3}$, making the temporal error subdominant the spatial error for $N \leq 12$. For $N > 12$, the temporal error dominates. The error in the velocity is measured in the energy norm, while the error in the pressure is measured in the L^2 norm. We clearly see exponential convergence in space.

Chapter 5

Buoyancy-driven flows

If a fluid is heated and the fluid density varies with temperature, a flow can be induced in the presence of gravity. This is known as buoyancy-driven flows. Many flow phenomena are driven by buoyancy, and such flows are important in a variety of engineering applications, e.g. ventilation in rooms, cooling of nuclear reactors and electronic components. The numerical examples throughout this paper will consist of such flow problems.

5.1 The Boussinesq approximation

When temperature gives rise to density variations, a full analysis of the flow problem gets quite complex, and we need an approximation. The most common choice is known as the Boussinesq approximation [8]. In the Boussinesq approximation the density differences are neglected, except in the buoyancy term where they appear in terms multiplied by g, the acceleration due to gravity. The gravity acting on the density variations provokes buoyancy forces which drives the fluid flow.

Let us now denote the constant density of the flow by ρ_0. If all accelerations involved in the flow are small compared to g, the dependence of the density on T in the buoyancy term can be considered as linear [2]:

$$\rho - \rho_0 = \Delta\rho = -\rho_0\beta(T - T_0).$$

Here, T_0 is a reference temperature, e.g. the temperature on a boundary, and β is the coefficient of expansion for the fluid defined as

$$\beta = -\frac{1}{\rho}\frac{\partial p}{\partial T}.$$

The corresponding buoyancy force is then given as

$$\boldsymbol{f}_B = \Delta\rho\boldsymbol{g} = -\rho_0\mathbf{g}\beta(T - T_0).$$

Hence, we can write the incompressible N-S equations for a buoyancy-driven flow as

$$\rho_0\Big(\frac{\partial \boldsymbol{u}}{\partial t} + \boldsymbol{u}\cdot\nabla\boldsymbol{u}\Big) - \mu\nabla^2\boldsymbol{u} + \nabla p = -\rho_0\boldsymbol{g}\beta(T - T_0), \tag{5.1}$$

$$\nabla\cdot\boldsymbol{u} = 0. \tag{5.2}$$

From (5.1) we see that one also requires an equation which describes the heat distribution. For this purpose we use the convection-diffusion equation described in Chapter 2. In terms of appropriate constants, we can state the energy equation as

$$\rho_0 c_p\Big(\frac{\partial T}{\partial t} + \boldsymbol{u}\cdot\nabla T\Big) = \kappa\nabla^2 T + q, \tag{5.3}$$

where q is the rate of internal heat generation per unit volume, and c_p and κ is the specific heat capacity and thermal conductivity for the fluid, respectively.

The equations (5.1)–(5.3) constitute the equations for a buoyancy-driven flow. Note that the velocity distribution is governed by both the pressure field and the temperature distribution, while the temperature distribution depends through the convection of heat on the velocity distribution. Hence, we have a coupled problem in velocity, pressure and temperature.

The behaviour of the systems depends upon the magnitude of the buoyancy force relative to the other terms in (5.1). We will in this paper consider the case in which the buoyancy force is the only cause of motion, called free or natural convection.

5.2 Benchmark problem: buoyancy-driven flow in a cavity

5.2.1 Problem description

We now consider fluid flow in a differentially heated closed square cavity, depicted in Figure 5.1. The left and right walls are maintained at temperatures T_H and T_C, respectively (assume $T_H > T_C$), while the horizontal walls are adiabatic, meaning that there is no heat transfer through these walls. The fluid inside the cavity is assumed to be incompressible, Newtonian and Boussinesq-approximated, and we assume no-slip conditions on the boundaries.

The governing equations are given by (5.1)–(5.3). For this problem, we assume no internal heat generation, and thus $q = 0$. If we set the reference temperature $T_0 = T_C$, we arrive at the following system of equations

$$\rho_0\Big(\frac{\partial \boldsymbol{u}}{\partial t} + \boldsymbol{u}\cdot\nabla\boldsymbol{u}\Big) - \mu\nabla^2\boldsymbol{u} + \nabla p = \boldsymbol{f}_B, \tag{5.4}$$

$$\rho_0 c_p\Big(\frac{\partial T}{\partial t} + \boldsymbol{u}\cdot\nabla T\Big) - k\nabla^2 T = 0, \tag{5.5}$$

$$\nabla\cdot\boldsymbol{u} = 0, \tag{5.6}$$

where the buoyancy force is given as $\boldsymbol{f}_B = -\rho_0\mathbf{g}\beta(T - T_C)$.

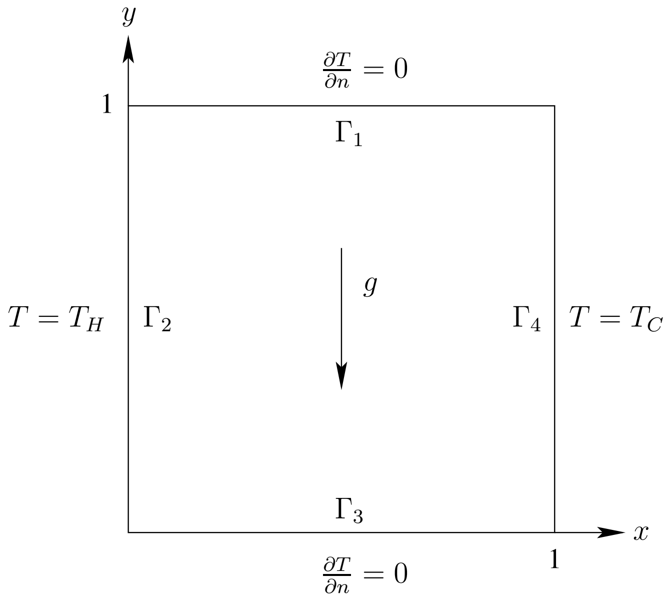

Figure 5.1: The computational domain Ω for the buoyancy-driven cavity.

The dimensionless form of the equations (5.4)–(5.6) can be obtained by applying the following non-dimensionalized variables [3]:

$$\begin{aligned}
\tilde{x} &= \frac{x}{L}, \quad \tilde{y} = \frac{y}{L}, \quad \tilde{u}_x = \frac{L}{\alpha}u_x, \quad \tilde{u}_y = \frac{L}{\alpha}u_y \\
\tilde{t} &= \frac{\alpha}{L^2}t, \quad \tilde{p} = \frac{L^2}{\rho_0\alpha^2}p, \quad \theta = \frac{T-T_C}{T_H-T_C},
\end{aligned}$$

where L is an appropriate length scale and α denotes the thermal diffusion rate given by $\kappa/\rho_0 c_p$. In terms of the non-dimensionalized variables, we now have the following set of equations

$$\begin{aligned}
\text{Incompressibility:} &\quad \tilde{\nabla}\cdot\tilde{\boldsymbol{u}} = 0, \\
x\text{-momentum:} &\quad \frac{\partial \tilde{u}_x}{\partial \tilde{t}} - \mathrm{Pr}\,\tilde{\nabla}^2\tilde{u}_x + \tilde{\boldsymbol{u}}\cdot\tilde{\nabla}\tilde{u}_x + \frac{\partial \tilde{p}}{\partial \tilde{x}} = 0, \\
y\text{-momentum:} &\quad \frac{\partial \tilde{u}_y}{\partial \tilde{t}} - \mathrm{Pr}\,\tilde{\nabla}^2\tilde{u}_y + \tilde{\boldsymbol{u}}\cdot\tilde{\nabla}\tilde{u}_y + \frac{\partial \tilde{p}}{\partial \tilde{y}} = \mathrm{Ra}\,\mathrm{Pr}\,\theta, \\
\text{Energy :} &\quad \frac{\partial \theta}{\partial \tilde{t}} + \tilde{\boldsymbol{u}}\cdot\tilde{\nabla}\theta - \tilde{\nabla}^2\theta = 0,
\end{aligned}$$

where the dimensionless numbers Ra and Pr are the Rayleigh number and the Prandtl number, respectively, defined as

$$\mathrm{Ra} = \frac{g\beta \Delta T L^3}{\alpha\nu} \quad \text{and} \quad \mathrm{Pr} = \frac{\nu}{\alpha}.$$

The Prandtl number represents the ratio of the momentum diffusivity and thermal diffusivity, while the Rayleigh number can be viewed as the ratio of buoyancy forces and thermal and momentum forces. In what follows, we set the Prandtl number equal to unity, and treat the Rayleigh number as the parameter of interest.

Note that the definition of the dimensionless temperature implies that

$$\theta|_{\Gamma_2} = 1, \quad \theta|_{\Gamma_4} = 0,$$

while the boundary conditions on Γ_1 and Γ_3 remain the same, i.e. homogeneous Neumann conditions. The boundary conditions for the dimensionless velocity also remain the same, i.e. pure homogeneous Dirichlet boundary conditions.

From now on we only consider the non-dimensionalized equations, and we drop the "$\sim$"-notation on the variables throughout the paper. Hence, the governing equations in non-dimensional form are written as

$$\frac{\partial \boldsymbol{u}}{\partial t} + \boldsymbol{u} \cdot \nabla \boldsymbol{u} - \nabla^2 \boldsymbol{u} + \nabla p = \boldsymbol{f}, \tag{5.7}$$

$$\nabla \cdot \boldsymbol{u} = 0, \tag{5.8}$$

$$\frac{\partial \theta}{\partial t} + \boldsymbol{u} \cdot \nabla \theta - \nabla^2 \theta = 0, \tag{5.9}$$

where $\boldsymbol{f}$ is given as

$$\boldsymbol{f} = \begin{bmatrix} 0 \\ \mathrm{Ra}\,\theta \end{bmatrix}.$$

To solve the equations (5.7)-(5.8), we use the results derived for the N-S equations in Section 4.2, while the results derived for the convection-diffusion equation in Chapter 2 are applied to solve (5.9). Hence, the resulting set of algebraic equations are given by

$$x\text{-velocity}: \quad \Big(\boldsymbol{B}\frac{S}{\Delta t} + \boldsymbol{A}\Big)\boldsymbol{u}_x^{n+1} - \boldsymbol{D}_x \boldsymbol{p}^{\star,n+1} = -(\boldsymbol{C}\boldsymbol{u}_x)^{\star,n+1}, \tag{5.10}$$

$$y\text{-velocity}: \quad \Big(\boldsymbol{B}\frac{S}{\Delta t} + \boldsymbol{A}\Big)\boldsymbol{u}_y^{n+1} - \boldsymbol{D}_x \boldsymbol{p}^{\star,n+1} = \mathrm{Ra}\,\boldsymbol{B}\boldsymbol{\theta}^n - (\boldsymbol{C}\boldsymbol{u}_y)^{\star,n+1}, \tag{5.11}$$

$$\text{Pressure}: \quad \boldsymbol{A}\boldsymbol{p}^{n+1} = \boldsymbol{h}^{n+1} - \boldsymbol{z}^{\star,n+1}, \tag{5.12}$$

$$\text{Temperature}: \quad \Big(\boldsymbol{B}\frac{S}{\Delta t} + \boldsymbol{A}\Big)\boldsymbol{\theta}^{n+1} = -(\boldsymbol{C}\boldsymbol{\theta})^{\star,n+1} - \boldsymbol{A}\boldsymbol{\theta}_b. \tag{5.13}$$

We now make a few remarks. On the right hand side of (5.13) we have an additional term $\boldsymbol{A}\boldsymbol{\theta}_b$ due to the inhomogeneous boundary conditions imposed on θ. Here, $\boldsymbol{\theta}_b$ is a vector with the inhomogeneous Dirichlet boundary values in the entries corresponding to grid nodes on Γ_2, and zeros in the remaining nodes.

We see that we need to solve three Helmholtz problems and one Poisson problem at each time step: first, we solve (5.10)-(5.11) for the velocity components, where both the pressure and the temperature are treated as known quantities. The updated velocity is then used to evaluate the right hand side of (5.12), and the corresponding Poisson problem is solved for the pressure. In the end, the temperature is updated from (5.13).

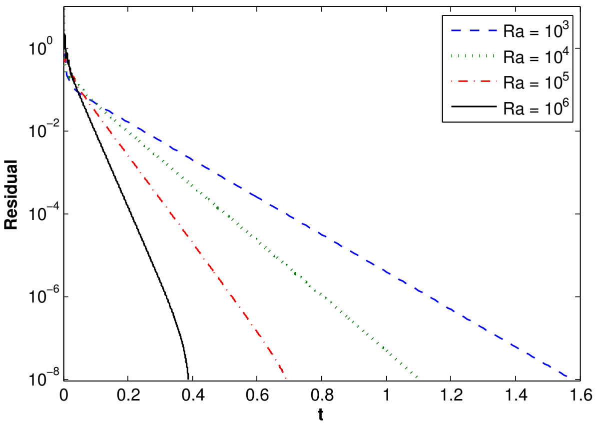

Figure 5.2: Residual for the energy equation as a function of dimensionless time. The system reaches a steady state faster as the Rayleigh number increases.

5.2.2 Numerical results

Convergence study

Unlike the problems earlier in this paper, the real size of the numerical error can never be computed for this problem, since there is no analytic solution available. However, it is possible to measure how close we are to a steady state solution.

When a steady state solution is reached, the time-derivative terms in the equations (5.7)–(5.9) should be zero. Hence, a steady state solution satisfies the following equations:

$$\boldsymbol{u} \cdot \nabla \boldsymbol{u} - \nabla^2 \boldsymbol{u} + \nabla p = \boldsymbol{f}, \tag{5.14}$$

$$\nabla \cdot \boldsymbol{u} = 0, \tag{5.15}$$

$$\boldsymbol{u} \cdot \nabla \theta - \nabla^2 \theta = 0, \tag{5.16}$$

While we integrate the system (5.10)-(5.13) in time, we can find a measure of how close we are to a steady state solution by inserting the present solution into the weak form of (5.14)–(5.16). By computing the residual, which we define as the Euclidean norm of the subtracted left and right hand side, we find a measure of how close we are to a steady state solution.

To ensure a steady state solution, we require the residual to be at least 10^{-8} in all simulations. In Figure 5.2 we see the convergence history of the residual for the temperature for different Rayleigh numbers. We see that the system reaches a steady state solution faster as the Rayleigh number increases. An explanation of this may be the growth in magnitude of the velocity field for increasing Rayleigh numbers, depicted in Figure 5.3 for the x-component. When the magnitude of the velocity increases, a fluid particle will move faster inside the cavity and reach a steady path at an earlier stage.

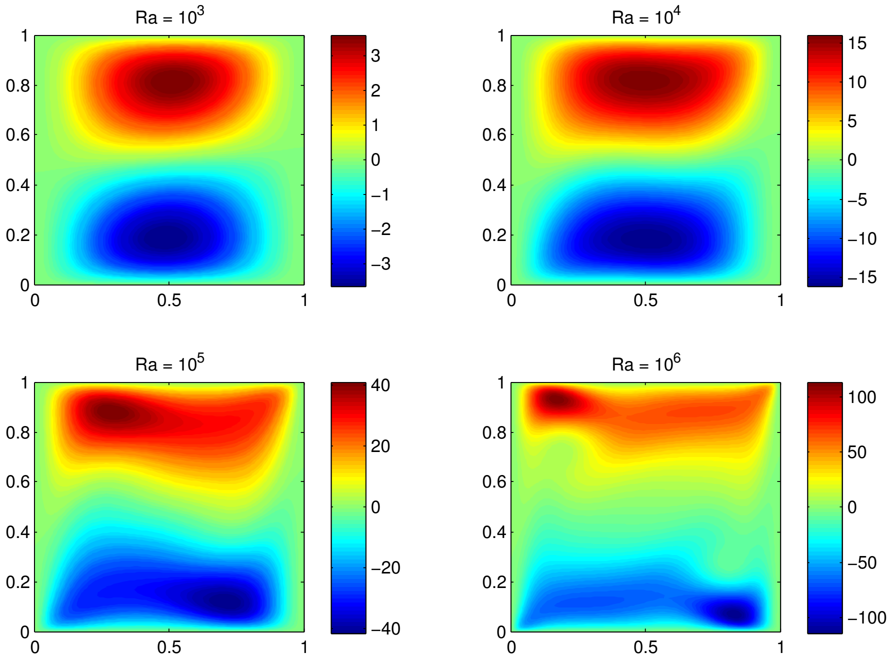

Figure 5.3: Isovelocity contours of the x-component for various Rayleigh numbers. We clearly see that the magnitude of the velocity increases with the Rayleigh number.

Flow patterns

To visualize the flow patterns, we need to be able to calculate the streamlines of the flow. We remark that the visualization of streamlines is not a built-in tool in Matlab, hence we need to make our own tool.

For an incompressible flow we know that $\nabla \cdot \boldsymbol{u} = 0$, which in two dimensions can be written as

$$\frac{\partial u_x}{\partial x} + \frac{\partial u_y}{\partial y} = 0.$$

We note that this equation is still satisfied if we introduce

$$u_x = \frac{\partial \psi}{\partial y}, \quad u_y = -\frac{\partial \psi}{\partial x}, \tag{5.17}$$

where ψ is known as the stream function. To derive an expression for the stream function we introduce the vorticity defined as $\boldsymbol{\omega} = \nabla \times \boldsymbol{u}$. The vorticity corresponds to the rotation of the fluid. In two dimensions, the vorticity is given as

$$\boldsymbol{\omega} = \underbrace{\left(\frac{\partial u_y}{\partial x} - \frac{\partial u_x}{\partial y}\right)}_{\omega} \boldsymbol{k},$$

where $\boldsymbol{k}$ is the unit vector in the z-direction, i.e. the third spatial direction. By using (5.17) we can write

$$\omega = -\frac{\partial^2 \psi}{\partial x^2} - \frac{\partial^2 \psi}{\partial y^2} = -\nabla^2 \psi.$$

Hence, we can find the stream function by solving the Poisson equation

$$-\nabla^2 \psi = \omega,$$

with homogeneous Neumann boundary conditions.

Lines of constant ψ are known as the streamlines of the flow. In two dimensions, streamlines are curves where

$$\frac{\mathrm{d}x}{u_x} = \frac{\mathrm{d}y}{u_y}.$$

To see why the stream function is constant at such curves, we consider the differential of ψ

$$\mathrm{d}\psi = \frac{\partial \psi}{\partial x}\mathrm{d}x + \frac{\partial \psi}{\partial y}\mathrm{d}y = -u_y \mathrm{d}x + u_x \mathrm{d}y = 0 \implies \frac{\mathrm{d}x}{u_x} = \frac{\mathrm{d}y}{u_y}.$$

Hence, we can depict the streamlines of the flow by plotting the contour lines of the stream function.

In Figure 5.4 we see the computed flow patterns at steady state for different Rayleigh numbers. The figure shows streamlines of the flow, isovelocity contours of both velocity components and isotherms, i.e. lines of constant temperature.

For the lowest Rayleigh number taken into count, we see from the streamlines the existence of a single circulating eddy. As the Rayleigh number increases, the circulation is divided into two counter-rotating eddies that decrease in magnitude and move towards the walls of constant temperature. We also see the formation of boundary layers at the isothermal walls in the higher Ra-range.

For $\mathrm{Ra} = 10^3$ the isotherms are close to normal to the vertical walls. However, as the Rayleigh number increases, the isotherms gradually becomes parallel to the adiabatic walls, and boundary layers are created along the isothermal walls.

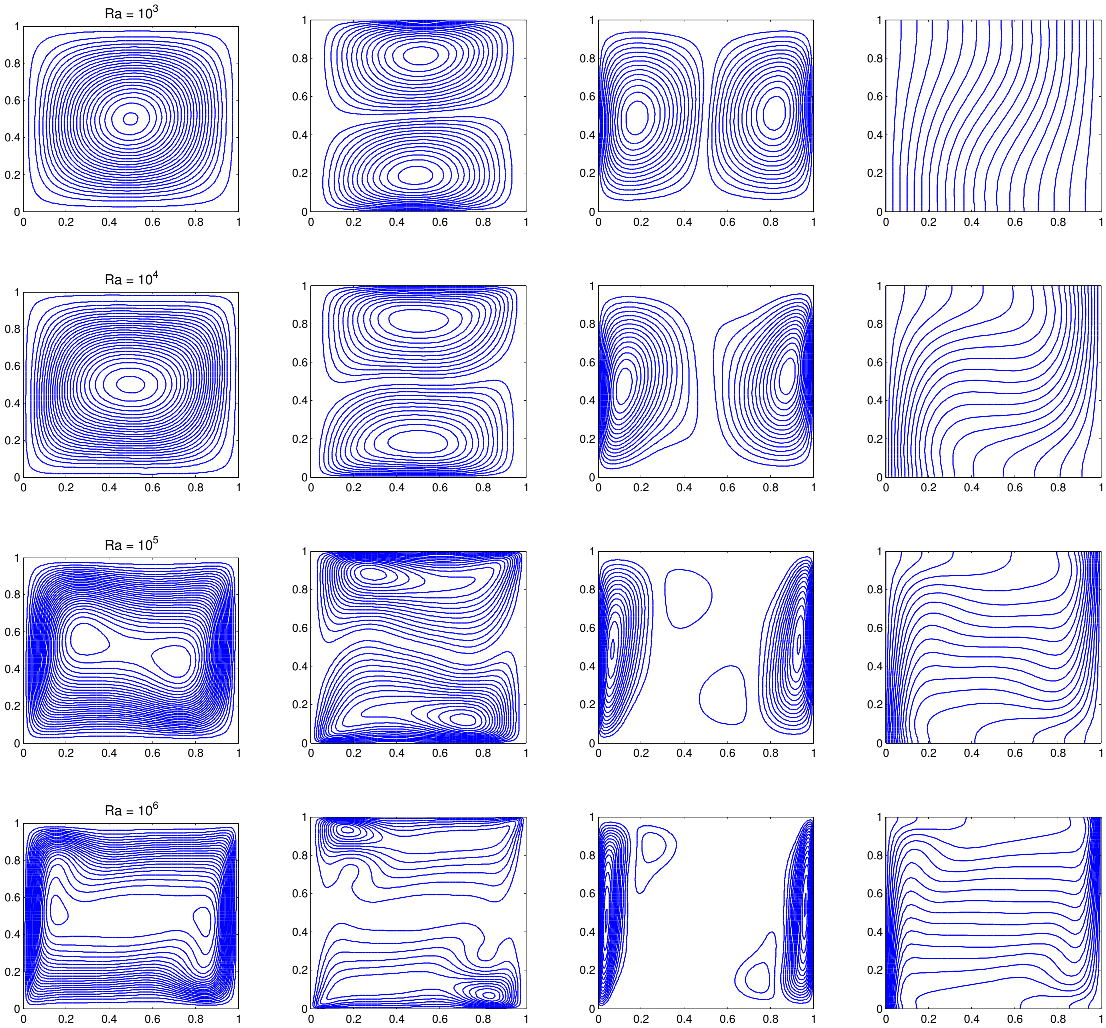

Figure 5.4: Computed steady state flow patterns of the buoyancy-driven cavity for different Rayleigh numbers. From the left: Streamlines, isovelocity contours of the x-component, isovelocity contours of the y-component and isotherms.

Thermal distribution: the Nusselt number

Knowledge of the rate of heat transfer along the hot and cold walls of differentially heated cavities may be valuable information for both engineers and designers. A quantity of particular interest, is the amount of heat transfered through a surface into or out of the fluid [2]. This quantity is given by the Nusselt number (Nu), which measures the ratio of heat transferred between the plates by a moving fluid to the heat transfer that would occur by pure conduction, i.e., if the fluid were stationary. For this particular problem, the non-dimensional Nusselt number is given by the following relation [10]:

$$\mathrm{Nu} = -\frac{\partial \theta}{\partial x}\bigg|_{\mathrm{wall}}. \tag{5.18}$$

The relation represents the local Nusselt number, which is defined in each spatial grid point on the considered wall. Due to the boundary conditions, the Nusselt number is non-zero only on the isothermal walls.

Note that the interpretation of the local Nusselt number is different for the hot and the cold wall. At the hot wall, the Nusselt number represents the heat transfer from the wall to the fluid, while it represents the heat transfer from the fluid to the wall at the cold wall.

As a result of the definition, the Nusselt number must satisfy the condition $\mathrm{Na} \geq 1$. Being a relative measure, the numerical value of the Nusselt number is minimal for pure conduction. For this case, the steady equation for the non-dimensional temperature reduces to

$$-\nabla^2 \theta = 0.$$

With the present boundary conditions, the solution is given by

$$\theta(x, y) = 1 - x,$$

resulting in the corresponding Nusselt number

$$\mathrm{Nu} = -\frac{\partial \theta}{\partial x}\bigg|_{\mathrm{wall}} = 1.$$

As a result of this, the Nusselt number is close to 1 for low Rayleigh numbers where the magnitude of the velocity field is small, while it increases with the Rayleigh number.

Another quantity of interest is the average Nusselt number, a parameter given by

$$\overline{\mathrm{Na}} = \int_\Gamma \mathrm{Nu}\,\mathrm{d}s = -\int_0^1 \frac{\partial \theta}{\partial x}\bigg|_{\mathrm{wall}} \mathrm{d}y.$$

There are different ways to carry out the computation for this parameter. One possible approach is to explicitly differentiate θ, and evaluate the integral by GLL quadrature. For instance, the average Nusselt number on the cold wall (Γ_4) can be computed as follows (recall that $L_x = L_y = 1$):

$$\begin{aligned}
\overline{\mathrm{Na}} &= -\int_0^1 \frac{\partial \theta}{\partial x}\Big|_{x=1} \mathrm{d}y \\
&= -\int_{-1}^1 \frac{\partial \hat{\theta}}{\partial \xi}\Big|_{\xi=1} \mathrm{d}\eta \\
&= -\sum_{m=0}^{N}\sum_{n=0}^{N} \theta_{mn} \underbrace{\ell_m'(1)}_{D_{Nm}} \Big(\int_{-1}^1 \ell_n(\eta)\,\mathrm{d}\eta \Big) \\
&\simeq -\sum_{m=0}^{N}\sum_{n=0}^{N} \theta_{mn} D_{Nm} \Big(\sum_{\alpha=0}^{N} \rho_\alpha \ell_n(\xi_\alpha) \Big) \\
&= -\sum_{m=0}^{N}\sum_{\alpha=0}^{N} \rho_\alpha \theta_{m\alpha} D_{Nm},
\end{aligned}$$

where $\boldsymbol{D}$ is a matrix where each element is the derivative of one of the Lagrangian interpolants at one of the GLL points, i.e. $D_{ij} = \ell_j'(\xi_i)$.

However, the results we present here are calculated using a more clever approach, which is based on the weak form of the underlying heat equation. In order to explain this approach, we consider the simplified steady heat transfer problem

$$-\nabla^2 \theta = f \quad \text{in} \quad \Omega, \tag{5.19}$$

$$\theta = 0 \quad \text{on} \quad \Gamma_2, \Gamma_4, \tag{5.20}$$

$$\frac{\partial \theta}{\partial n} = 0 \quad \text{on} \quad \Gamma_1, \Gamma_3. \tag{5.21}$$

Even if this problem is simplified compared to the full energy equation (in which our model is based on), it illustrates the idea of the procedure, and the extension to the full energy equation is straightforward.

As a point of departure, we define the corresponding weak formulation of (5.19)-(5.21). Defining the space $X = \{v \in H^1(\Omega) \mid v|_{\Gamma_2} = 0, v|_{\Gamma_4} = 0\}$, the weak problem can be stated as: find $v \in X$ such that

$$a(\theta, v) = (f, v), \quad \forall v \in X.$$

Discretizing this problem by the Legendre spectral method, we end up with the following system of algebraic equations:

$$\boldsymbol{A}\,\boldsymbol{\theta} = \boldsymbol{B}\boldsymbol{f}, \tag{5.22}$$

where $\boldsymbol{A}, \boldsymbol{B} \in \mathbb{R}^{(N^2-1)\times(N^2-1)}$ and $\boldsymbol{\theta}, \boldsymbol{f} \in \mathbb{R}^{(N^2-1)}$.

Suppose now that we are to compute the average Nusselt number on Γ_4. In order to do this, we introduce a modified problem where the homogeneous Dirichlet condition on Γ_4 is changed to an inhomogeneous Neumann condition, i.e.

$$\begin{aligned} -\nabla^2\theta &= f \quad \text{in} \quad \Omega, \\ \theta &= 0 \quad \text{on} \quad \Gamma_2, \\ \frac{\partial\theta}{\partial n} &= 0 \quad \text{on} \quad \Gamma_1, \Gamma_3, \\ \frac{\partial\theta}{\partial n} &= g \quad \text{on} \quad \Gamma_4. \end{aligned}$$

Defining the space $X^\star = \{v \in H^1(\Omega) \mid v|_{\Gamma_2} = 0\}$, the corresponding weak problem can be stated as: find $\theta^\star \in X^\star$ such that

$$a(\theta^\star, v) = (f, v) + l(v), \quad \forall v \in X^\star, \tag{5.23}$$

where $l(\cdot)$ is the linear form associated with the inhomogeneous Neumann condition:

$$l(v) = \int_{\Gamma_4} g\, v \,\mathrm{d}s = \int_{\Gamma_4} \frac{\partial\theta}{\partial n} v \,\mathrm{d}s.$$

Note that, for any $v \in X^\star$ such that $v\Big|_{\Gamma_4} = 1$,

$$\begin{aligned} -l(v) &= -\int_{\Gamma_4} g \,\mathrm{d}s \\ &= -\int_{\Gamma_4} \frac{\partial\theta}{\partial n} \,\mathrm{d}s \\ &= -\int_0^1 \frac{\partial\theta}{\partial x} \,\mathrm{d}y = \overline{\mathrm{Na}}. \end{aligned}$$

Now, consider the case when $\theta = \theta^\star$, i.e., the heat transfer is adjusted such that $\theta^\star|_{\Gamma_4} = 0$. Inserting this into (5.23), we get

$$-l(v) = (f, v) - a(\theta, v) = r, \quad \forall v \in X^\star. \tag{5.24}$$

Note that r will be zero everywhere except on Γ_2 and Γ_4. If we discretize (5.24), we end up with the following system of equations.

$$\boldsymbol{r} = \boldsymbol{B}^\star \boldsymbol{f}^\star - \boldsymbol{A}^\star \boldsymbol{\theta}^\star, \tag{5.25}$$

where $\boldsymbol{A}^\star, \boldsymbol{B}^\star \in \mathbb{R}^{N(N+1)\times N(N+1)}$ and $\boldsymbol{\theta}^\star, \boldsymbol{f}^\star \in \mathbb{R}^{N(N+1)}$. Since $X \subset X^\star$, the solution $\boldsymbol{\theta}^\star$ can be found by extending the solution of (5.22) by zeros on grid points corresponding to the boundary Γ_4.

Recall that we need to choose $v \in X^\star$ such that $v|_{\Gamma_4} = 1$. However, this is simply the test functions associated with the nodes on Γ_4. Hence, we can find the average Nusselt number on Γ_4 by

$$\overline{\mathrm{Na}}|_{\Gamma_4} = \sum_{i=0}^{N} r_{Ni}.$$

For the flow problem we consider here, where the domain is a simple rectangle, the difference between the two approaches are small both in terms of computational cost and accuracy. However, for deformed geometries, the weak form approach is superior to the explicit differentiation approach [9]. If we evaluate the line integral by quadrature, we have to compute normal vectors of all the grid points along the boundary that we want to find the heat transfer through. Even if this is fully computable, it will demand a lot of work, and the implementation will be quite elaborate.

In Table 5.1 the computed average Nusselt numbers for different Rayleigh numbers are listed, together with the minimum and maximum local Nusselt numbers. Similar results from [10], [14] are also listed for comparison. We see that the computed values agree well with other results, verifying a correct solution.

In Figure 5.5 we see the distribution of the local Nusselt number at the hot and the cold wall for various Rayleigh numbers. For the lowest Rayleigh number taken into account, we see that the local Nusselt number is close to unity at every grid point, implying that the heat transfer is mainly due to conduction. For the higher Ra-range, where the effect of convection is more significant, the Nusselt number is clearly increasing with the Rayleigh number, as expected.

Note that for the hot wall, there is greater heat transfer from the lower part of the wall to the fluid, while for the cold wall, there is greater heat transfer from the fluid to the wall at the upper part of the wall. We also see that there is an anti-symmetric distribution of the local Nusselt number between the hot and cold wall. This is as expected due to the anti-symmetric distribution of the steady fluid flow and the isotherms in Figure 5.4.

Table 5.1: Maximum, minimum and average local Nusselt number for different values of Ra.

		Computed			[14]			[10]	
Ra	Max	Min	$\overline{\text{Na}}$	Max	Min	$\overline{\text{Na}}$	Max	Min	$\overline{\text{Na}}$
10^3	1.507	0.691	1.117	1.506	0.691	1.115	1.501	0.691	1.117
10^4	3.582	0.579	2.256	3.531	0.585	2.259	3.579	0.577	2.254
10^5	7.965	0.711	4.600	7.708	0.728	4.483	7.945	0.698	4.598
10^6	18.082	0.952	9.087	17.531	0.985	8.881	17.860	0.913	8.976

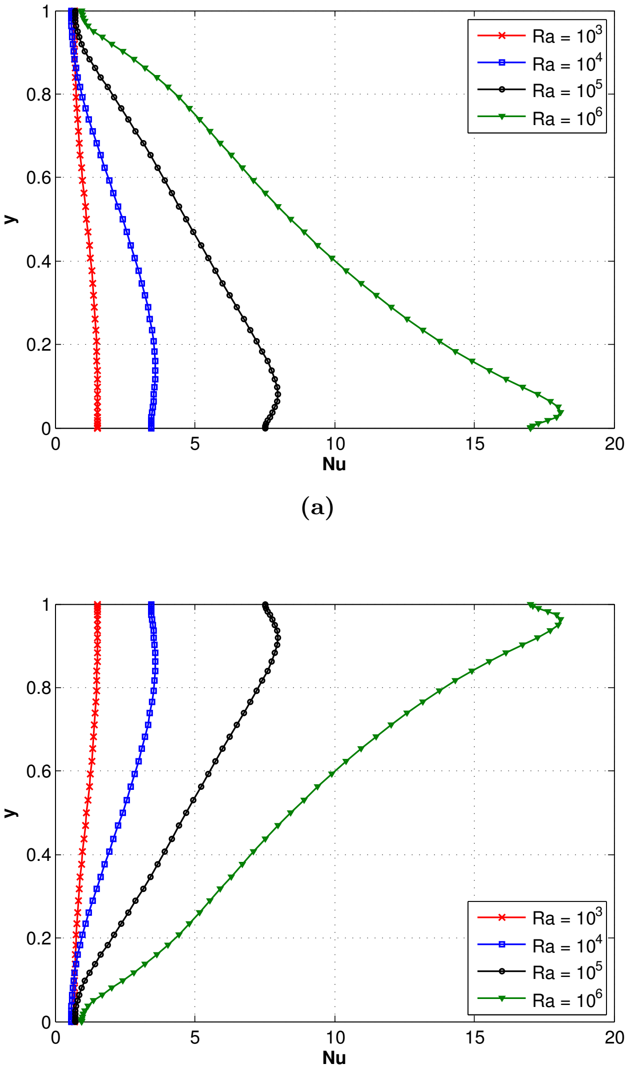

(a)

(b)

Figure 5.5: Distribution of the local Nusselt number for different Rayleigh numbers. In a) we see the distribution for the hot wall, while b) shows the distribution for the cold wall.

5.3 Rayleigh–Bénard convection

Rayleigh–Bénard convection is a phenomenon that may occur in a layer of fluid between two isothermal horizontal plates, where a temperature difference exists between the plates. The first experimental observations was made by Henry Bénard in the early 1900s [17].

If the temperature of the upper plate is higher than the lower plate, the lighter hot fluid is situated above the heavy cold fluid. Hence, the fluid is stable and no flow occurs. If we turn the situation around, i.e., if the lower plate is maintained at a higher temperature than the upper plate, the fluid at the bottom will be lighter than the fluid at the top. In this case, the cold fluid tends to move downwards, while the hot fluid tends to move upwards, causing a potentially unstable arrangement. However, this tendency of movement will be opposed by the fluids own viscosity.

Evidently, the temperature difference between the plates is not the only criterion for motion to occur. Like the flow in the differentially heated cavity, the Rayleigh–Bénard convection is highly dependent on the dimensionless Rayleigh number. The name of the parameter is a result of the theoretical foundation laid by Lord Rayleigh: by applying linear stability theory, Rayleigh was able to show that the stability of the system depends on the numerical value of the Rayleigh number.

A linear stability analysis may be performed as follows: starting from a flow that is a stationary state solution of the system, each physical variable is slightly perturbed, i.e., each variable is increased infinitesimally. This will result in a new set of equations governing these increments. The linearized equations is then obtained by neglecting all products and higher powers of the increments, leaving only the linear terms.

To test the system's stability, the system needs to be exposed to every possible perturbation. This can be accomplished by expressing an arbitrary perturbation as a superposition of basic modes, and test the system with respect to each of these modes. We do not explain the method in detail here, but the reader is referred to [20] for a further discussion.

From the linear stability theory, Rayleigh discovered that for Rayleigh numbers smaller than a critical value, the viscous force dominates the buoyancy force, and no flow is observed. However, as the Rayleigh number exceeds a critical value, the buoyancy force is stronger than the viscous force and we experience onset of convection. The critical value of the Rayleigh number depends on the boundary conditions on the upper and lower walls, which may be either free, rigid walls or a combination of those. We will consider the case with rigid walls, where the critical value is known to be $\mathrm{Ra}_c = 1707.8$ [20, 16].

The shape of the convected flow pattern is typically a series of parallel counter-rotating rolls (see Figure 5.6). A pair of counter-rotating rolls have length λ, and the critical length corresponding to the critical Rayleigh number Ra_c is given by $\lambda_c = 2.016$.

Like we did for the differentially heated cavity, we assume the fluid between the rigid walls to be incompressible, Newtonian and Boussinesq-approximated. Hence, the governing equations in non-dimensionalized variables are given by ($\mathrm{Pr} = 1$)

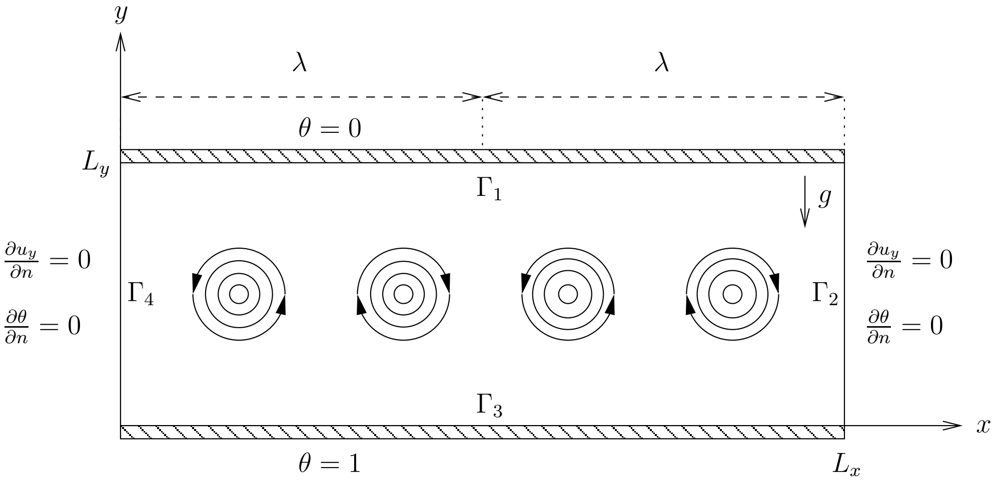

Figure 5.6: The geometry of Rayleigh–Bénard convection. A layer of fluid is kept between two isothermal horizontal rigid plates where the lowest plate is maintained at the highest temperature. For Ra $>$ Ra$_c$ we experience onset of convection, and parallel counter-rotating rolls are observed. The boundary conditions for non-dimensionalized variables are also given. If nothing else is specified, the boundary conditions for the velocity components are homogeneous Dirichlet.

$$\begin{aligned}
\text{Incompressibility:}\quad & \nabla \cdot \boldsymbol{u} = 0, \\
x\text{-momentum:}\quad & \frac{\partial u_x}{\partial t} - \nabla^2 u_x + \boldsymbol{u} \cdot \nabla u_x + \frac{\partial p}{\partial x} = 0, \\
y\text{-momentum:}\quad & \frac{\partial u_y}{\partial t} - \nabla^2 u_y + \boldsymbol{u} \cdot \nabla u_y + \frac{\partial p}{\partial y} = \mathrm{Ra}\,\theta, \\
\text{Energy:}\quad & \frac{\partial \theta}{\partial t} + \boldsymbol{u} \cdot \nabla \theta + \nabla^2 \theta = 0.
\end{aligned}$$

The boundary conditions for the problem is given in Figure 5.6. Note that we now consider different boundary conditions for the two velocity components. By imposing homogeneous Neumann conditions on the adiabatic walls for the y-component of the velocity, we create an effect of slippery walls with low friction, making the model more realistic.

To solve the equations, we use exactly the same approach as for the differentially heated cavity (see Section 5.2.1). The only difference is a slight change in the boundary conditions.

5.3.1 Numerical results

In Figure 5.7 we see the computed steady state flow pattern of Rayleigh–Bénard convection for $L_x = 2\lambda_c$, $L_y = 1$ and $\mathrm{Ra} = 2000$. We clearly see two pairs of rolls, as expected, while the vector field verifies that the rolls are in fact counter-rotating. For comparison, a picture of a real Rayleigh–Bénard experiment from Van Dyke [19] is included.

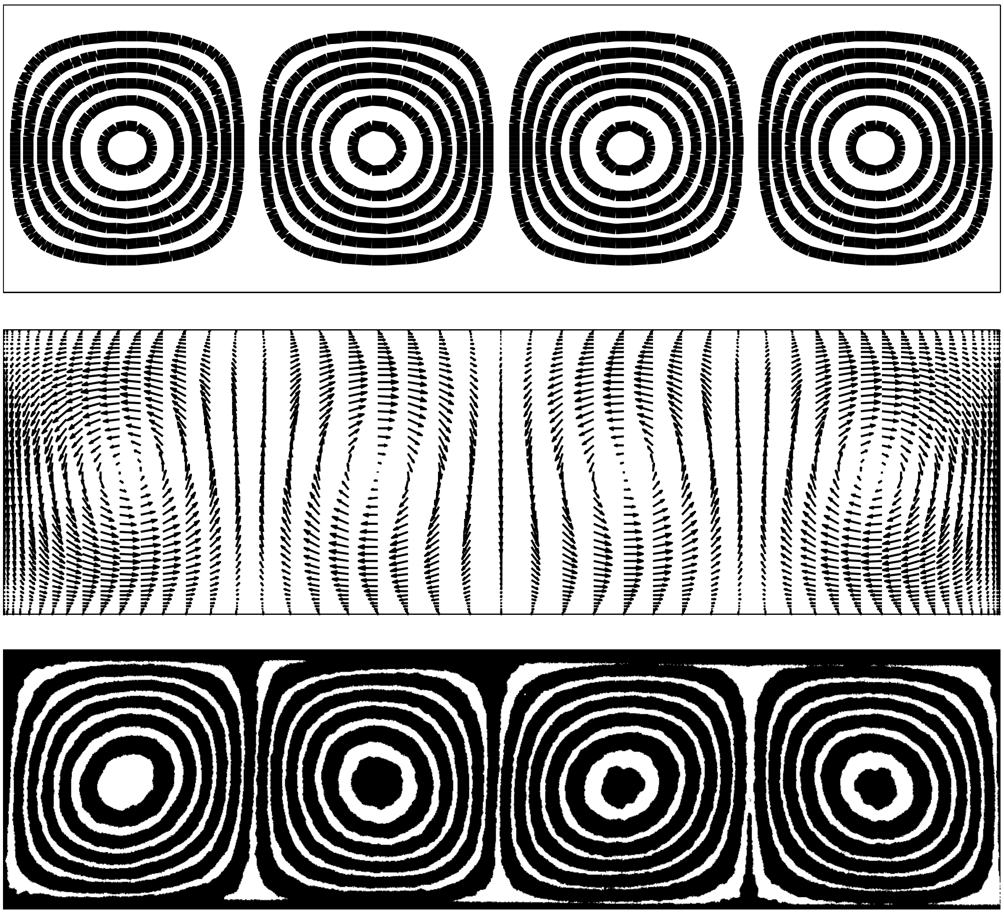

Figure 5.7: Steady state flow patterns of the Rayleigh–Bénard convection with slippery vertical boundaries. The parameters used are Ra = 2000, $L_x = 2\lambda_c$ $L_x = 1$. From the top: computed streamlines, computed vector field and a picture from [19] of a real Rayleigh–Bénard experiment.

In order to determine the critical Rayleigh number for our model, we consider the energy of the velocity field. As a measure for the energy, we use the L^2 norm of the velocity field:

$$E = ||\boldsymbol{u}||_{L^2(\Omega)} = \Big(\int_\Omega (u_x^2 + u_y^2)\, \mathrm{d}\Omega \Big)^{\frac{1}{2}}.$$

Since the magnitude of the velocity field increases with the Rayleigh number, we expect the energy to go to zero as we approach the critical Rayleigh number from above. At the critical Rayleigh number there is no motion in the fluid, and the energy is equal to zero. In Figure 5.8 we see the energy as a function of the Rayleigh number. From the figure we see that the critical Rayleigh number is in the region $\mathrm{Ra}_c \in (1705, 1710)$. By refining the time step and by carrying out results for the Rayleigh numbers in this region, the numerical value of the critical Rayleigh number for this model is found to be $\mathrm{Ra}_c^* \approx 1707.4$. This result is in good agreement with the theoretical result by Rayleigh.

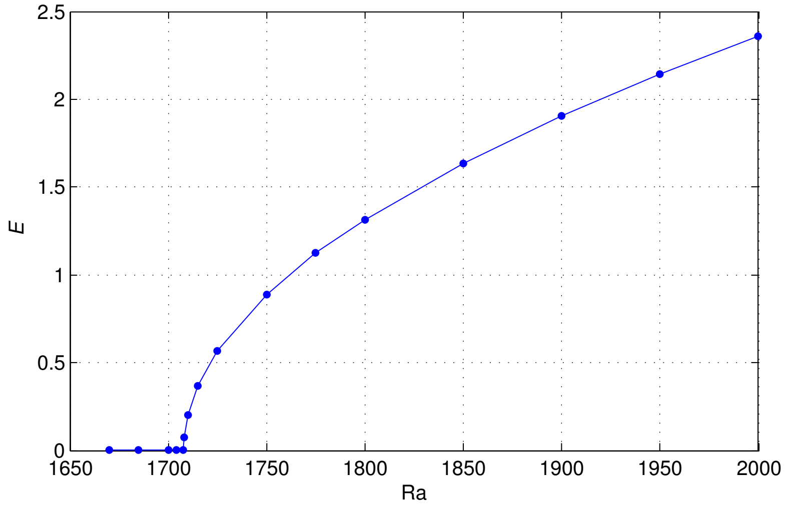

Figure 5.8: The L^2 norm of the steady state velocity field as a function of the Rayleigh number for slippery vertical boundaries. The parameters used are $L_x = \lambda_c, L_y = 1$.

It is also interesting to consider the case where we impose no-slip conditions at all the boundaries of the computational domain, i.e., pure homogeneous Dirichlet boundary conditions for the velocity components. In such case, the slippery conditions at the vertical boundaries no longer hold, and there is more friction involved. The computed streamlines with such boundary conditions are depicted in Figure 5.9. Here, the parameters used are $\mathrm{Ra} = 2500, L_x = 2\lambda_c$ and $L_y = 1$. We see that the rolls differ in magnitude, with the inner rolls stronger than the outer rolls. The outer rolls are also somewhat compressed compared to the inner rolls, due to the friction at the vertical walls.

Due to the increase in friction, we expect the buoyancy force to be stronger for convection to occur in this case. Hence, we expect a larger critical Rayleigh number for this model. In Figure 5.10 we see the energy of the velocity field as a function of the Rayleigh number. To determine the critical Rayleigh number, we use the same approach as for the case with slippery walls: we refine the time step in the region where the energy is approximately zero. For this case, the critical Rayleigh number is found to be $\mathrm{Ra}_c^* \approx 2005$, which is significantly higher than the value we found for slippery walls.

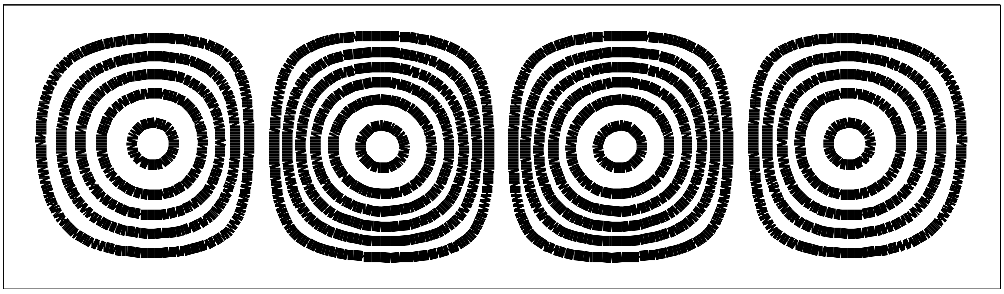

Figure 5.9: Computed steady state streamlines of Rayleigh–Bénard convection with pure homogeneous Dirichlet boundary conditions for both velocity components. The parameters used are Ra $=$ 2500, $L_x = 2\lambda_c$ and $L_y = 1$.

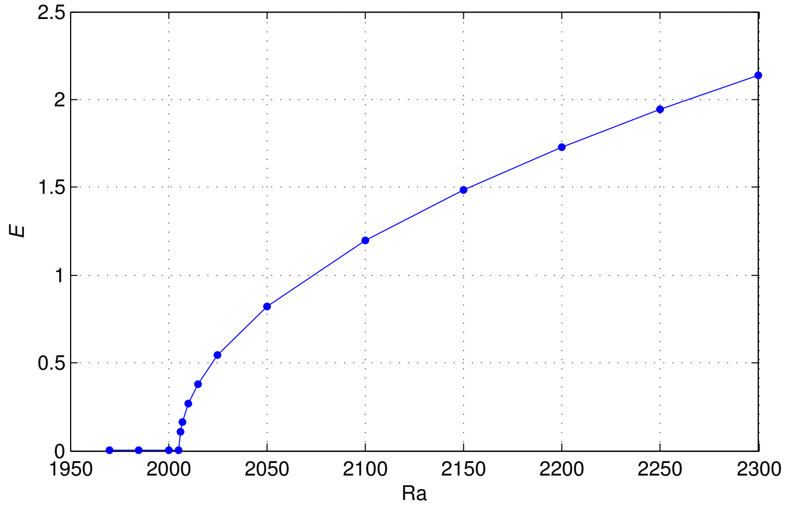

Figure 5.10: The L^2 norm of the steady state velocity field as a function of the Rayleigh number for pure no-slip conditions. The parameters used are $L_x = \lambda_c, L_y = 1$.

Chapter 6

Conclusions

In this report, a Legendre spectral method in space and operator splitting methods in time has been employed to solve buoyancy-driven flow problems in two-dimensional enclosures. In particular, we have considered flow in a differentially heated cavity and an example of Rayleigh–Bénard convection.

In Section 2 we presented a solution of the two-dimensional convection-diffusion equation. Both the spatial and the temporal discretization methods were carefully explained, and we presented a solution of the arising Helmholtz-type set of algebraic equations. By exploiting the simple geometry of the problem and the properties of the tensor product, we were able to derive a direct solver of the Helmholtz problem in only $\mathcal{O}(N^3)$ floating point operations and $\mathcal{O}(N^2)$ storage requirement. For comparison, a direct approach using Gaussian elimination would require $\mathcal{O}(N^6)$ floating point operations and $\mathcal{O}(N^4)$ storage requirement.

In the following chapter, the unsteady Stokes problem was solved by applying an operator splitting discretization scheme. The scheme is based on a weak form of the pressure Poisson equation, and at each time-step one only has to solve a set of Helmholtz-type equations for each velocity component and a Poisson equation for the pressure. By employing the derived Helmholtz solver to the arising system of equations, the scheme provides a fast solver that is relatively easy to implement. The expected convergence rates of both the spatial and the temporal discretization were also verified.

An extension of the Stokes splitting scheme was applied to solve the incompressible unsteady Navier–Stokes equations. By using a Boussinesq approximation for the coupled fluid-thermal problem, we derived the equations that govern buoyancy-driven flows. In the first problem, we put emphasis on the arising thermal distribution, quantified by the local and the average Nusselt number. To evaluate the average Nusselt number, we presented a useful technique in which the connection between Dirichlet and Neumann boundary conditions is exploited. This approach avoids computation of temperature gradients, and provides high-accuracy results. The computed results of both the local and the average Nusselt number agreed well with earlier numerical computations, and verified the correctness of the overall implementation.

For the Rayleigh–Bénard problem, we computed the characteristic streamlines of the flow, which are observed as a series of parallel counter-rotating rolls. The effect of the non-dimensional Rayleigh number was studied, as the parameter decides whether we experience onset of convection or not. By measuring the energy of the velocity field, and by making use of the fact that the energy is zero for sub-critical Rayleigh numbers, we determined the critical Rayleigh number for our model to be $\mathrm{Ra}_c^* = 1707.4$. This result agrees well with previous published results from linear stability theory, where the critical value is determined to be $\mathrm{Ra}_c = 1707.8$.

In summary, the splitting scheme considered in this paper appears to be a suitable tool for numerical solution of incompressible flow problems. The splitting scheme enjoys desirable properties such as a fully decoupling of the velocity and the pressure and the possibility of achieving exponential convergence in space, even if the discretization spaces does not satisfy the inf-sup condition. This, combined with the efficient solvers available for the arising system of algebraic equations, makes the discretization scheme well suited for buoyancy-driven flows in rectangular domains.

Bibliography

[1] J.L. Guermnond and J. Shen. A new class of truly consistent splitting schemes for incompressible flows. *ScienceDirect, Journal of Computational Physics*, Vol. 192, Pages 262-276, 2003.

[2] D.J. Tritton. *Physical fluid dynamics, second edition.* Oxford University Press, 1988.

[3] R.D.C. Oliveski, M.H. Macagnan and J.B. Copetti. Entropy generation and natural convection in rectangular cavities. *ScienceDirect, Applied Thermal Engineering*, Vol. 29, Pages 1417-1425, 2008.

[4] C. Canuto, M.Y. Hussaini, A. Quarteroni and T.A. Zang. *Spectral Methods in Fluid Dynamics*, Springer-Verlag, 1988

[5] C. Bernardi and Y. Maday. Spectral, Spectral Element and Mortar Element Methods in *Theory and Numerics of Differential Equations.* Edited by J.F. Blowey, J.P. Coleman and A.W. Craig. Springer-Verlag, 2001.

[6] M.O. Deville, P.F. Fischer and E.H. Mund. *High-order Methods for Incompressible Fluid Flow.* Cambridge University Press, 2002.

[7] M. Massoud. *Engineering Thermofluids : Thermodynamics, Fluid Mechanics, and Heat Transfer.* Springer Berlin Heidelberg, 2005.

[8] A. Bejan and A.D. Krauss. *Heat Transfer Handbook.* John Wiley & Sons , 2003.

[9] G. F. Carey, Derivative calculation from finite element solutions. *Computer Methods in Applied Mechanics and Engineering* , Vol 35, No. 1, pages 1-14, 1982.

[10] D.C. Wan, B.S.V. Patnaik and G.W. Wei, A new benchmark quality solution for the buoyancy-driven cavity by discrete singular convolution. *Taylor & Francis, Numerical Heat Transfer* , Part B, Vol. 40, pages 199-228, 2001.

[11] G. Karniadakis, J. Sherwin. *Spectral/hp element methods for CFD.* Oxford University Press, 1999.

[12] C. Foias. *Navier-Stokes equations and turbulence.* Cambridge University Press, 2001.

[13] M.T. Manzari, An explicit finite element algorithm for convection heat transfer problems. *International Journal of Numerical Methods for Heat & Fluid Flow,*, Vol. 9, No. 8, pages 860-877, 1999.

[14] D.A. Mayne, A.S. Usmani and M. Crapper, h-adaptive finite element solution of high Rayleigh number thermally driven cavity problem. *International Journal of Numerical Methods for Heat & Fluid Flow,*Vol. 10, No. 6, pages 598-615, 2000.

[15] P.D. Minev, F.N. Van de Vosse, L.J.P. Timmermans and A.A. Van Steenhoven, A second order splitting algorithm for thermally-driven flow problems. *International Journal of Numerical Methods for Heat & Fluid Flow,*Vol. 6, No. 2, pages 51-60, 1995.

[16] S.E. Norris. *A Parallel Navier Stokes Solver for Natural Convection and Free Surface Flow.* University of Sydney. Engineering, 2006.

[17] A. Pellew and R.V. Southwell. On maintained convective motion in a fluid heated from below. *Proceedings of the Royal Society of London. Series A, Mathematical and Physical Sciences,* Vol. 176, No. 966, pages 312-343, 1940.

[18] N. Ouertatani, N.B. Cheikh, B.B. Beya and T. Lili. Numerical simulation of two-dimensional Rayleigh–Bénard convection in an enclosure. *ScienceDirect, C.R. Mecanique,*Vol. 336, pages 464-470, 2008.

[19] M. Van Dyke. *An Album of Fluid Motion.* The Parabolic Press, Stanford, California, 1982.

[20] S. Chandrasekhar. *Hydrodynamic and Hydromagnetic Stability.* Oxford University Press, 1961.

[21] J.T. Lir and T.F. Lin. Visualization of roll patterns in Rayleigh–Bénard convection of air in a rectangular shallow cavity. *International Journal of Heat and Mass Transfer,* Vol. 44, pages 2889-2902, 2001.

[22] J. Pallares, I. Cuesta and F.X. Grau. Laminar and turbulent Rayleigh–Bénard convection in a perfectly conducting cubical cavity. *ScienceDirect, International Journal of Heat and Fluid Flow,* Vol. 23, pages 346-358, 2002.

[23] C. Canuto, M.Y. Hussaini, A. Quarteroni and T.A. Zang. *Spectral Methods - Evolution to Complex Geometries and Applications to Fluid Dynamics.* Springer Berlin Heidelberg, 2007.

[24] G.E. Karniadakis, M. Israeli and S.A. Orszag. High-Order Splitting Methods for the Incompressible Navier–Stokes Equations. *Journal of Computational Physics* , Vol. 97, pages 414-443, 1991.

Appendix A

A.1 Gauss–Lobatto–Legendre quadrature

Gauss–Lobatto–Legendre (GLL) quadrature is a method for numerical integration. For GLL quadrature we have the following result [4]:

$$\int_{\widehat{\Omega}} g(\xi,\eta)\,\mathrm{d}\xi\,\mathrm{d}\eta = \sum_{\alpha=0}^{N}\sum_{\beta=0}^{N} \rho_\alpha \rho_\beta \; g(\xi_\alpha, \xi_\beta), \quad \forall g \in \mathbb{P}_{2N-1}(\widehat{\Omega}), \quad \widehat{\Omega} = (-1,1)^2.$$

Here $\{\rho_i\}_{i=0}^{N}$ are one-dimensional quadrature weights and $\{\xi\}_{i=0}^{N}$ are one-dimensional quadrature points. We see that GLL quadrature is exact for all polynomials of degree less than or equal to $2N-1$ over the domain $\widehat{\Omega} = (-1,1)^2$.

The $N+1$ one-dimensional GLL points are obtained as roots of the equation

$$(1-x^2)L_N'(x) = 0,$$

where $L_N'(x)$ denotes the first order derivative of the N-th order Legendre polynomial.

A.2 Tensor product

For two general matrices $\boldsymbol{A} \in \mathbb{R}^{n_1 \times n_2}$ and $\boldsymbol{B} \in \mathbb{R}^{n_3 \times n_4}$, we define the tensor product as

$$\boldsymbol{C} = \boldsymbol{A} \otimes \boldsymbol{B} \in \mathbb{R}^{n_1 n_3 \times n_2 n_4},$$

with matrix elements

$$\boldsymbol{C} = \begin{bmatrix} A_{11}\boldsymbol{B} & A_{12}\boldsymbol{B} & \cdots & A_{1n_2}\boldsymbol{B} \\ \vdots & & & \vdots \\ A_{n_1 1}\boldsymbol{B} & A_{n_1 2}\boldsymbol{B} & \cdots & A_{n_1 n_2}\boldsymbol{B} \end{bmatrix}$$

The tensor product has the following properties:

(i)

$$(\boldsymbol{A} \otimes \boldsymbol{B})(\boldsymbol{C} \otimes \boldsymbol{D}) = (\boldsymbol{A}\boldsymbol{C} \otimes \boldsymbol{B}\boldsymbol{D}),$$

(ii)

$$\boldsymbol{A} = (\boldsymbol{B} \otimes \boldsymbol{C}) \implies \boldsymbol{A}^{-1} = (\boldsymbol{B}^{-1} \otimes \boldsymbol{C}^{-1}),$$

(iii)

$$\boldsymbol{A} = (\boldsymbol{B} \otimes \boldsymbol{C}) = (\boldsymbol{B} \otimes \boldsymbol{I})(\boldsymbol{I} \otimes \boldsymbol{C}),$$

where $\boldsymbol{I}$ is the identity operator.

(iv) If $\boldsymbol{A}, \boldsymbol{B}$ are diagonal, so is $\boldsymbol{C} = (\boldsymbol{A} \otimes \boldsymbol{B})$.